ADVANCED FUNCTIONAL MATERIALS
www.afm-journal.de

Advanced Characterization and Optimization of NiO_x:Cu-SAM Hole-Transporting Bi-Layer for 23.4% Efficient Monolithic Cu(In,Ga)Se_2-Perovskite Tandem Solar Cells

Ivona Kafedjiska, Igal Levine, Artem Musiienko, Natalia Maticiuc, Tobias Bertram, Amran Al-Ashouri, Christian A. Kaufmann, Steve Albrecht, Rutger Schlatmann, and Iver Lauermann**

The performance of five hole-transporting layers (HTLs) is investigated in both single-junction perovskite and Cu(In, Ga)Se_2 (CIGSe)-perovskite tandem solar cells: nickel oxide (NiO_x,), copper-doped nickel oxide (NiO_x:Cu), NiO_x+SAM, NiO_x:Cu+SAM, and SAM, where SAM is the [2-(3,-6Dimethoxy-9H-carbazol-9yl)ethyl]phosphonic acid (MeO-2PACz) self-assembled monolayer. The performance of the devices is correlated to the charge-carrier dynamics at the HTL/perovskite interface and the limiting factors of these HTLs are analyzed by performing time-resolved and absolute photoluminescence ((Tr)PL), transient surface photovoltage (tr-SPV), and X-ray/UV photoemission spectroscopy (XPS/UPS) measurements on indium tin oxide (ITO)/HTL/perovskite and CIGSe/HTL/perovskite stacks. A high quasi-Fermi level splitting to open-circuit (QFLS-V_{oc}) deficit is detected for the NiO_x-based devices, attributed to electron trapping and poor hole extraction at the NiO_x-perovskite interface and a low carrier effective lifetime in the bulk of the perovskite. Simultaneously, doping the NiO_x with 2% Cu and passivating its surface with MeO-2PACz suppresses the electron trapping, enhances the holes extraction, reduces the non-radiative interfacial recombination, and improves the band alignment. Due to this superior interfacial charge-carrier dynamics, NiO_x:Cu+SAM is found to be the most suitable HTL for the monolithic CIGSe-perovskite tandem devices, enabling a power-conversion efficiency (*PCE*) of 23.4%, V_{oc} of 1.72V, and a fill factor (*FF*) of 71%, while the remaining four HTLs suffer from prominent V_{oc} and *FF* losses.

1. Introduction

Metal-halide perovskites with a general formula ABX_3 (**A**: cation like methyl ammonium, cesium or formamidinium; **B**: Pb^{2+}, or Sn^{2+}; **X**: I^-, or Br^-) have quickly become one of the most popular absorber materials for solar cells and have yielded single-junction solar-cells efficiencies above 25%.[1] The metal-halide perovskite photo-absorbers are known for their direct and tunable bandgap,[2] high defect tolerance,[3,4] and suitability for monolithic-tandem integration.[5,6] Moreover, integrating a wide-bangap perovskite as an add-on, top cell on either silicon (Si) or copper-indium-gallium-diselenide (Cu(In,Ga)Se_2, CIGSe) in a monolithic tandem configuration is an attractive approach to decrease the thermalization losses in the Si or CIGSe single-junction devices and overcome their detailed balance limit of efficiency.[7]

By now, the monolithic Si-perovskite and CIGSe-perovskite tandem solar cells have reached efficiencies as high as 33.2%[1] and 24.2%,[8] respectively. Although the CIGSe solar cells, same as the perovskite-based solar cells, exhibit a direct and tunable

I. Kafedjiska, N. Maticiuc, T. Bertram, C. A. Kaufmann, R. Schlatmann, I. Lauermann
Helmholtz-Zentrum Berlin für Materialien und Energie GmbH
Kompetenzzentrum Photovoltaik Berlin (PVcomB)
Schwarzschildstraße 3, 12489 Berlin, Germany
E-mail: ivona.kafedjiska@helmholtz-berlin.de;
iver.lauermann@helmholtz-berlin.de

The ORCID identification number(s) for the author(s) of this article can be found under https://doi.org/10.1002/adfm.202302924

DOI: 10.1002/adfm.202302924

I. Levine, A. Musiienko
Helmholtz-Zentrum Berlin für Materialien und Energie GmbH
Institut Silizium-Photovoltaik
Kekuléstraße 5, 12489 Berlin, Germany

A. Al-Ashouri, S. Albrecht
Helmholtz-Zentrum Berlin für Materialien und Energie GmbH
Institut Silizium-Photovoltaik
HySPRINT Innovation Lab, Kekuléstraße 5, 12489 Berlin, Germany

S. Albrecht
Technical University Berlin
Faculty of Electrical Engineering and Computer Science
Marchstraße 23, 10587 Berlin, Germany

R. Schlatmann
Hochschule für Technik und Wirtschaft
Faculty 1 - Energy and Information
HTW Berlin, 10313 Berlin, Germany

bandgap,[9] are cheap to be manufactured and can be deposited on flexible substrates suitable for building-integrated photovoltaics,[10,11] their integration into the perovskite-based monolithic tandems has been hindered by the non-negligible surface roughness of the CIGSe cell. Since the top device is currently predominantly deposited via solution-processing techniques, the underlying rough surface can possibly lead to poorer shunt resistance even in the best-performing tandem solar cells, as seen by the current certified world-record device.[8]

One way to overcome this challenge is to co-evaporate CI(G)Se absorbers with substantially decreased surface roughness, as demonstrated by the certified CIS-based 23.35%-efficient device developed by [12]. However, this approach is not very attractive for large-scale and industrial applications since the current certified world-record single-junction CIGSe device is obtained with a sequentially-processed CIGSe absorber with a non-negligible surface roughness.[13]

Another approach would be to incorporate mechanical polishing of the bottom-cell surface until a smooth surface is obtained, as demonstrated by the 22.4%-efficient tandem in [14]. However, this high efficiency was obtained for a very small active area of 0.04cm^2, while increasing the area to 0.5cm^2 already led to a decrease of the PCE down to 20.8%.[14] The pronounced loss in efficiency as the active area was increased indicates that the mechanical polishing of the bottom cell is a cumbersome approach, unsuitable for up-scaling of the monolithic CIGSe-perovskite tandem solar cells.

Therefore, the most industrially-attractive approach would be to use native, rough absorbers and then investigate and optimize the hole-transporting layer (HTL), which is deposited on top of the bottom CIGSe cell and below the top perovskite solar cell. The optimal HTL would ensure conformal coverage of the bottom cell, an efficient carrier extraction, and suppress the non-radiative recombination at the HTL-perovskite interface. In the tandem solar cells, the HTL additionally plays a crucial role in the formation of the desired recombination junction with the underlying material, thus ensuring an effective recombination of holes from the perovskite top cell with the electrons from the bottom cell.[15] Finally, the HTL plays a significant role in the stability[16] and up-scaling of the perovskites solar cells.[17]

Former research on the monolithic CIGS-perovskite tandems has focused on implementing organic HTLs such as PEDOT:PSS (poly(3,4-ethylenedioxythiophene):poly(styrene sulfonate))[18] or PTAA (poly[bis(4-phenyl)(2,4,6-trimethylphenyl)amine).[14] However, these HTLs can be unstable and are additionally expensive and unsuitable for the rough CIGS surface. The first promising progress in the field of HTL development for the monolithic CIGS-perovskite tandem solar cells was seen with the implementation of an atomic-layer deposited ALD NiO_x + PTAA HTL bi-layer on a cell area of 0.8cm^2 when a *FF* of ≈76%, V_{oc} of 1.58V, and a *PCE* of 21.6% was achieved.[19]

In 2018 the field of HTLs for perovskite solar cells was fully revolutionized by the introduction of a novel, organic self-assembled monolayer (SAM) which overcame many of the above-mentioned issues of the other organic HTLs.[20] For instance, a MeO-2PACz ([2-(3,6-dimethoxy-9H-carbazol-9-yl)ethyl]phosphonic acid) SAM yielded a *PCE* of 23.3% on a cell area >1cm^2 in a monolithic CIGSe-perovskite tandem solar cell.[5] Soon after, this performance was surpassed and the current certified world-record 24.2%-efficient monolithic CIGSe-perovskite solar cell with a Me-4PACz ([4-(3,6-dimethyl-9H-carbazol-9-yl)butyl] phosphonic acid) SAM as a stand-alone HTL and with a V_{oc} of 1.77V and a *FF* of 71.2% was manufactured.[8]

Despite this outstanding performance, this world-record tandem solar cell has a lower shunt resistance and *FF* compared to the 21.6%-efficient tandem solar cell with NiO_x + PTAA as an HTL,[19] motivating us to further explore the NiO_x potential for the tandem devices. Additionally, NiO_x has shown promising results in terms of its stability in air,[21,22] good optoelectronic properties,[23] and cheap manufacturing via various techniques[24–28]—characteristics which has made NiO_x to become one of the most-investigated inorganic HTL for perovskite solar cells applications.[23]

Therefore, this work addresses three important aspects for the implementation of NiO_x in the monolithic CIGSe-perovskite tandem solar cells. First, it aims to investigate the suitability of NiO_x-based HTLs in the tandem solar cells with co-evaporated CIGSe with a non-negligible surface roughness as the bottom sub-cell. Second, since the in-depth understanding on what truly limits the NiO_x-perovskite interface in the monolithic CIGSe-perovskite tandem solar cells is so far lacking, our work also systematically investigates its main limitations in terms of the interfacial charge-carrier dynamics via various advanced characterization methods. Last, but not least, since the ALD NiO_x used in the 21.6%-efficient monolithic CIGSe-perovskite tandem solar cell[19] required high-temperature annealing[29] unsuitable for the temperature-sensitive bottom CIGSe device, our work presents the first implementation of low-temperature radio frequency (RF) sputtered NiO_x from a NiO_x target in the monolithic CIGSe-perovskite tandem solar cells.

One of the highest-reported PCEs for magnetron-sputtered NiO_x at temperatures < 100°C in p-i-n single-junction perovskite devices with negligible hysteresis is 17.6% for a $MAPbI_3$ perovskite.[25] Reactively-sputtered NiO_x (with or without PTAA surface passivation) from a Ni target has been implemented in monolithic CIGS-perovskite solar cells only once, but the performance of the tandem solar cells did not exceed 16%.[30] One possible reason for the tandems' poor performance could be the difficulty to sputter NiO_x from a metallic Ni target and optimize the Ni^{3+}/Ni^{2+} (Ni_2O_3/NiO) ratio, which determines the optoelectronic properties of the NiO_x film.[31] Therefore, sputtering from a NiO_x target, as we do in this work, is a much more easily controllable process. This is also confirmed by Hou et al. who have followed the sputtering process in pure argon atmosphere described by Aydin et al.[25] to manufacture monolithic Si-perovskite tandem solar cells on textured crystalline silicon, obtaining a certified PCE of 25.7% and a promising stability over 400 h under continuous MPP tracking at 85° and at 45% to 50% relative humidity.[32]

However, it is questionable if low-temperature sputtered NiO_x can act as a stand-alone HTL in the perovskite-based (tandem) solar cells in its pristine form, since NiO_x-based single-junction perovskite devices are notoriously known for their V_{oc} losses. There are varying hypothesis as to what causes the V_{oc} loss in the NiO_x-based perovskite cells, ranging from poor selectivity of the NiO_x,[33] or dissatisfactory perovskite crystallization due to an excess of PbI_2 caused by an excess of Ni^{3+} species, as shown by Pant et. al[34–36] and similarly by Boyd et al.[37]

Despite the different approaches, these studies do have one common conclusion: the excess of the Ni^{3+} species is responsible for the NiO_x's high defect density, which, in turn, speeds up the recombination and negatively impacts the NiO_x-perovskite interface.

The two most-common approaches to address this issue and improve the V_{oc} in the NiO_x-based perovskite solar cells are to either dope the NiO_x, or to passivate the defects on the NiO_x-perovskite interface.

NiO_x has successfully been doped with zinc,[38] lithium,[39–41] cesium,[42] potassium,[43] magnesium,[44] and copper.[45–47] Champion p-i-n single-junction $MAPbI_3$ solar cells with low-temperature solution-processed NiO_x have been achieved by incorporating 5% Cu in a NiO_x solution.[48] Extensive XPS analysis showed that the detected improvements in the NiO_x work function, carrier concentration, and conductivity occur predominantly because Cu^{2+} species occupy Ni^{2+} vacancies ($V_{Ni^{2+}}$). Additionally, TrPL measurements indicated that NiO_x:Cu enabled more efficient charge extraction and a longer effective lifetime, finally resulting in a 20.26%-efficient champion device on rigid and a 17.4%-efficient device on flexible substrates with an area of 1 and 0.08cm^2, respectively.[48] In another work, high-temperature pulsed laser deposited (PLD) NiO_x with or without 3% Cu doping has also enabled a PCE of 20.41% and 18.65%, respectively in p-i-n single-junction solar cells in an fluorine-doped tin oxide (FTO)/NiO_x(:Cu)/chloride-doped formamidinium methylammonium lead iodide ($FA_{0.2}MA_{0.8}PbI_xCl_{3-x}$)/ [6,6]-phenyl-C61-butyric acid methyl ester (PCBM) / Rhodamine B (RhB) / lithium fluoride (LiF) / silver (Ag) stack.[49] Therefore, Cu is the only NiO_x's dopant that has enabled a PCE > 20% in single-junction perovskite solar cell, making it the most promising dopant researched in literature.

In addition to doping of the NiO_x, extensively different approaches have been adopted to passivate the NiO_x-perovskite interface.[50–69] Which surface treatment is adopted can also vary depending on which deposition technique has been used to deposit the NiO_x. Thus, potassium chloride[68] and various alkali metal-halide salts[63] were adopted for sputtered NiO_x; and a hybrid magnesium-organic interlayer for passivation of solution-processed NiO_x.[70] In addition to these interlayers, surface passivation with organic HTLs, such as spiro-OMeTAD (2,2′7,7′-tetrakis[N,N-di(4-methoxyphenyl)amino]-9-9′-spirobifluorene)[60] or PTAA[71] have also been investigated, but this approach has the downside of introducing possibly unstable and expensive organic molecules unsuitable for large-scale applications.

However, the surface passivation of the NiO_x with organic HTLs is not completely out of the question if self-assembled monolayers (SAMs) are used. So far, various SAMs with varying anchoring groups have been shown to successfully reduce possible recombination centers at the HTL-perovskite interface by saturating defects at the surfaces of various metal oxides (MO) which come in contact with the perovskite absorber. The SAM-based chemical passivation has also been shown to induce changes in the MO's work function (WF) by inducing a dipole moment;[72,73] by passivating some of the MO's oxygen vacancies or perovskite defects through chemical bonding;[74–76] by affecting the perovskite crystal growth;[77] or, by accelerating the charge extraction at the MO-perovskite interface.[78]

Specifically for the SAMs with phosphonic anchoring groups, it has been shown that compared to other organic HTLs, they are significantly cheaper, yield superior solar cell performance and stability, and display excellent compatibility for monolithic perovskite-based tandem devices,[6] as demonstrated by the world-record CIGSe-perovskite monolithic tandem solar cell[8] and the >29%-efficient monolithic Si-perovskite solar cells.[79] Moreover, SAMs have been shown to yield high efficiencies in monolithic textured Si-perovskite tandem solar cells when deposited on top of NiO_x, yielding a NiO_x + SAM HTL bi-layer configuration.[32,80]

Literature suggests that self-assembled monolayers with phosphonic anchoring groups like 2PACz ([2-(9H-carbazol-9-yl)ethyl]phosphonic acid) and Me-4PACz ([4-(3,6- dimethyl-9H-carbazol-9-yl)butyl]phosphonic acid) are superior in performance to MeO-2PACz ([2-(3,6-dimethoxy-9H-carbazol-9-yl)ethyl]phosphonic acid), primarily due to much lower dipole moment across the MeO-2PACz layer and better band alignment to the perovskite.[5,81] However, the combination of MeO-2PACz with NiO_x has already been shown to yield more reproducible solar-cell performance than MeO-2PACz as a stand-alone HTL, without inducing any V_{oc} losses.[82]

Motivated by the V_{oc} improvements via doping or SAM-based surface passivation of the NiO_x, in our previous research, we have looked into the performance of NiO_x with or without copper doping with SAM MeO-2PACz surface passivation in monolithic CIGS-perovskite tandem solar cells with two different types of CIGS absorbers: co-evaporated $Cu(In,Ga)Se_2$ and rapid-thermal processed $Cu(In,Ga)(S,Se)_2$.[83] The latter absorber is an industrially-attractive choice with a surface roughness twice as high as the co-evaporated $Cu(In,Ga)Se_2$ absorbers. Despite this high surface roughness, we have demonstrated a 21.6%-efficient proof of concept, industrially-attractive $Cu(In,Ga)(S,Se)_2$-perovskite monolithic tandem, which—due to the integration of NiO_x:Cu + SAM as a hole transporting bilayer—exhibits promising values for the *FF* and the V_{oc}.[83] This result is a new milestone for the monolithic CIGS-perovskite tandem solar cells since it shows that when the HTL is suitably optimized, an underlying rough CIGS surface does not have to limit the performance of the tandems. This study was followed-up with an investigation of the *FF* limitations in monolithic $Cu(In,Ga)Se_2$-perovskite tandem solar cells.[84] By performing a series of spectroscopic and imaging studies, we have identified that the *FF* in these tandems can be limited either by the hole-transporting layer, by the bottom, or by the top device, but understanding where the shunt is formed is not a straight forward task.[84]

Despite these findings, the charge-carrier dynamics at the interface, as well as the question why NiO_x:Cu + SAM is a better performing HTL than NiO_x + SAM, remain open topics. Hence, in this work we investigate thoroughly the performance of *five HTLs* in both inverted (p-i-n) single-junction perovskite and monolithic $Cu(In,Ga)Se_2$-perovskite tandem solar cells: four NiO_x-based HTL configurations (NiO_x, NiO_x:Cu, NiO_x + MeO-2PACz and NiO_x:Cu + MeO-2PACz) and MeO-2PACz as a stand-alone HTL. Altering the NiO_x-perovskite interface in such a stepwise manner, first by Cu doping and then by SAM passivation, enables us to gain deeper understanding into the NiO_x-perovskite interfacial charge-carrier dynamics and the dominating

physical mechanisms that play a role during the NiO_x doping or surface passivation. Since the open-circuit voltage (V_{oc}) is one of the main limiting factors of the NiO_x-based perovskite solar cells, we pay special attention to its variations in the solar cells. By combining devices' data with transient surface photovoltage (tr-SPV), time-resolved photoluminescence (TrPL), spectroscopic (XPS and UPS) measurements, as well as tr-SPV simulations, we find that the combination of MeO-2PACz with NiO_x:Cu can lead to the highest V_{oc} in the tandems. The substantial V_{oc} improvement is ascribed to the low interface trap density, low recombination rate, fast charge extraction, and favorable energetic alignment of the NiO_x:Cu-SAM bi-layer in the CIGSe-perovskite tandem solar cells, eventually yielding a promising efficiency of 23.4%.

Taking all of this into consideration, our study presents—to the best of our knowledge—the first systematic investigation of the charge-carrier dynamics of NiO_x and NiO_x:Cu with and without MeO-2PACz surface passivation in single-junction perovskite and monolithic CIGSe-perovskite tandem devices. By correlating the devices' data to the charge-carrier dynamics and the band alignment, we discuss the limitations of the NiO_x-based HTLs, as well as what needs to be understood before and during their optimization for monolithic tandem applications. Additionally, by introducing NiO_x(:Cu)-SAM bilayers as HTL in the CIGSe-perovskite monolithic tandem solar cells, we believe that we can diminish the possible risk of shunting during upscaling of the SAM-only tandems. Last, but not least, we also point out that any development in the HTL configuration for the CIGSe-perovskite tandems can be easily transferred to the textured Si surfaces as well, especially since by looking at the current Si-perovskite monolithic tandem record,[1] it is not too far-fetched to assume that the textured Si surface will be unavoidable in the future.

2. Results and Discussion

The results are divided into four main subsections: 1) performance of inverted (p-i-n) single junction perovskite and CIGSe-perovskite tandem solar cells; 2) investigation of the charge-carrier dynamics at the HTL-perovskite interface by transient surface photovoltage (tr-SPV), photoluminesence (PL) and time-resolved photoluminesence (TrPL) studies; 3) simulation of the tr-SPV data; and, 4) surface chemistry and electronic band alignment by XPS and UPS studies.

2.1. Performance of Inverted (p-i-n) Single Junction Perovskite and CIGSe-Perovskite Tandem Solar Cells With Varying HTLs

In **Figure 1**a,b, we present the solar-cell stack and exemplary *JV* curves respectively for single-junction p-i-n perovskite solar cells. In Figure 1c–e, we present the solar-cell stack, exemplary *JV* curves, and representative EQE measurements respectively for monolithic CIGSe-perovskite tandem solar cells. A cross-sectional SEM view of the tandem devices as well as an AFM measurement of the CIGSe absorber ($\sigma_{RMS} \approx 75$nm) are shown in Supporting Information.

Both the single-junction and tandem solar cells are manufactured with the five hole-transporting layer configurations: NiO_x, NiO_x:Cu, NiO_x+SAM, NiO_x:Cu+SAM and SAM as a stand-alone HTL, where SAM is consistently the MeO-2PACz self-assembled monolayer. We have opted for using MeO-2PACz instead of the more-commonly used PACz since our preliminary studies showed that the NiO_x(:Cu) + MeO-2PACz HTL bi-layer is a more promising configuration than the NiO_x(:Cu) + PACz HTL bi-layer configuration, which exhibited V_{oc} and *FF* losses (see Supporting Information).

We point out that the SAM-based tandem devices have around 3mA cm^{-2} lower current density compared to the other four devices due to an unfortunate change in the bandgap of the underlying CIGSe cell (as seen by the EQE measurements in Figure 1e) from around 1.06 to around 1.1eV. However, this small alteration in the bandgap would not influence significantly the parameters we are primarily interested in: the tandems' V_{oc} and *FF*. Nevertheless, for completeness, a theoretical *JV* curve has been presented in Figure 1d with a dashed violet line under the condition that the J_{sc} matches the J_{sc} of the other devices, but the *FF* and the V_{oc} remain unchanged. Under this assumption, the champion *JV* curve with SAM would have had a power conversion efficiency (*PCE*) of around 21.5%.

The EQE signals and the J_{sc} values of the four tandems with NiO_x(:Cu) with or without SAM surface passivation coincide well with one another within the measurement error (see Supporting Information). Still, we do detected small variations in the J_{sc} values across these four samples and we ascribe these to marginally varying optics - as detected in the 1-R measurements per HTL configuration (see Supporting Information). The optics might alter because of a slightly different absorption and crystallinity of the underlying HTLs (see Supporting Information for XRD and UV-vis measurements of the NiO_x(:Cu)), but also because of possible variations in the substrate roughness across the different CIGSe sub-cells which then affects the bulk properties of the perovskite.[85]

However, the tandem device with SAM (MeO-2PACz) as a stand-alone HTL displays a prominent J_{sc} drop of 2mA cm^{-2} for the top and 3mA cm^{-2} for the bottom sub-cell compared to the remaining four tandems. The reason for this J_{sc} loss is due to the following two reasons.

First, for the bottom/CIGSe sub-cell, the J_{sc} loss is ascribed to the different red response of this bottom cell compared to the other four CIGSe cells. As already mentioned, the CIGSe cell used in these tandems was mistakenly manufactured with a different gallium (Ga) back gradient, resulting in an altered bandgap as displayed by the EQE plot, and consecutively, a lowered J_{sc} value.

Second, for the top/perovskite sub-cell, the different underlying surface of the bottom device might affect the morphology of the top device up to an extent,[85] resulting in decreased J_{sc} . However, as we will discuss through this article, an even more prominent reason for the J_{sc} loss is the poor charge-carrier dynamics of SAM in the tandems. Compared to the tandems with NiO_x(:Cu) with or without SAM, SAM as a stand-alone HTL leads to the poorest hole extraction in the tandems, resulting in a reduced EQE signal across all wavelengths and thus, a reduced J_{sc} across all of the top cell. In addition to the representative *JV* curves, we also present a statistics for the reproducibility of the devices' performance per HTL configuration in forward- and reverse-bias scan direction: forty four small-area (0.16cm^2)

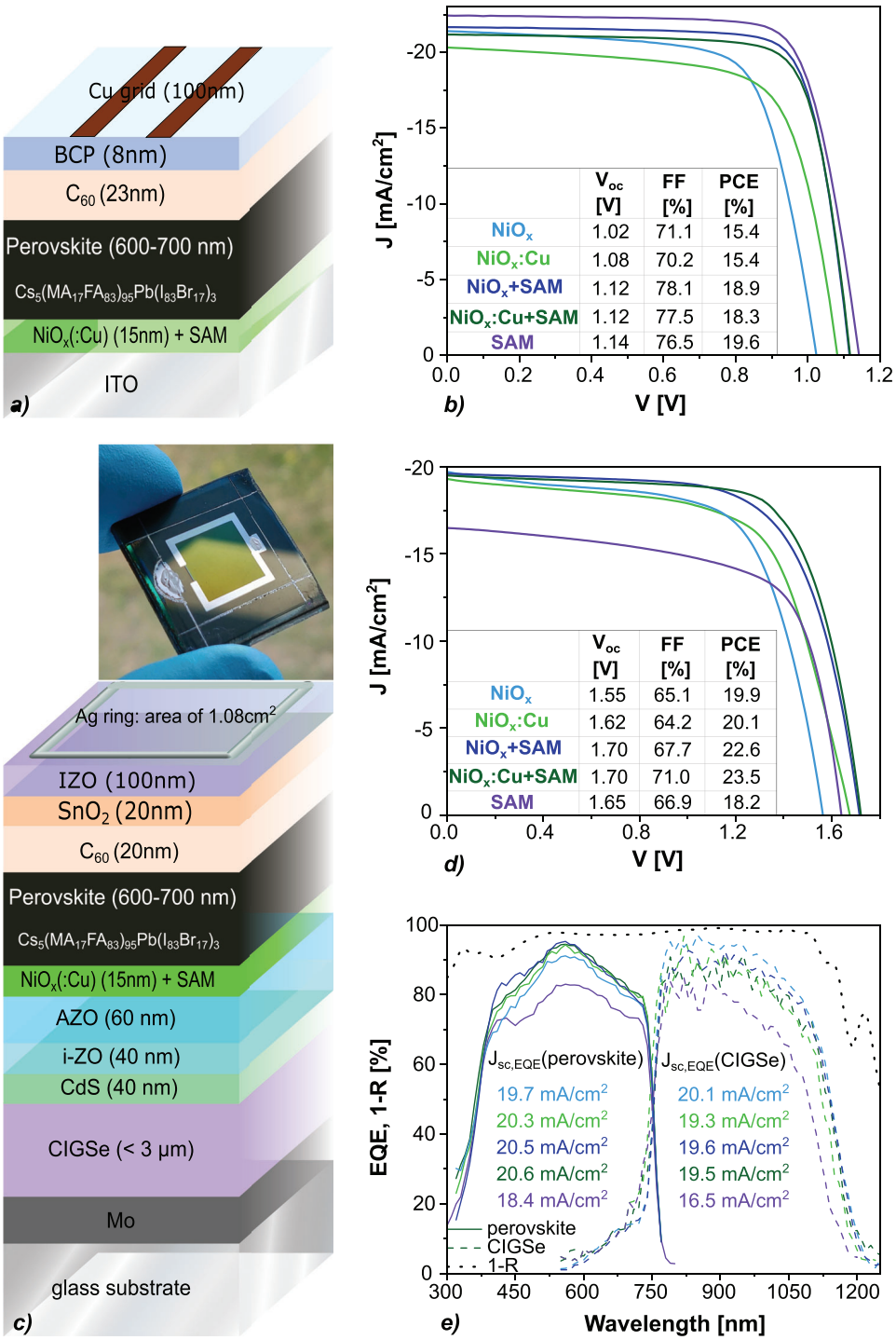

Figure 1. a,c) Sketch of the single-junction p-i-n perovskite solar cell and the monolitch CIGSe-perovskite tandem solar cell, respectively and a top-view photograph of the complete tandem solar cell (c). Light comes from the ITO or IZO side during measurement for the single-junction and tandem solar cell, respectively; b) Representative *JV* curves for single-junction perovskite solar cells and d) CIGSe-perovskite monolithic tandem solar cells; e) EQE measurements of the representative tandem solar cells.

devices per HTL configuration for the perovskite single-junction solar cells (**Figure 2**a–c), and three to four tandem devices with an area of 1.08cm^2 per HTL configuration. This modest number of tandem devices already gives us a first glimpse into the emerging trends among the solar-cells parameters and enables us to investigate the charge-carrier dynamics at the interfaces, as we will discuss later in Subsection 2.2. All of the *JV* curves (single-junction perovskite and CIGSe and monolithic CIGSe-perovskite tandem solar cells) can be found in Supporting Information. When cross-comparing the cells' performances for the single junctions and

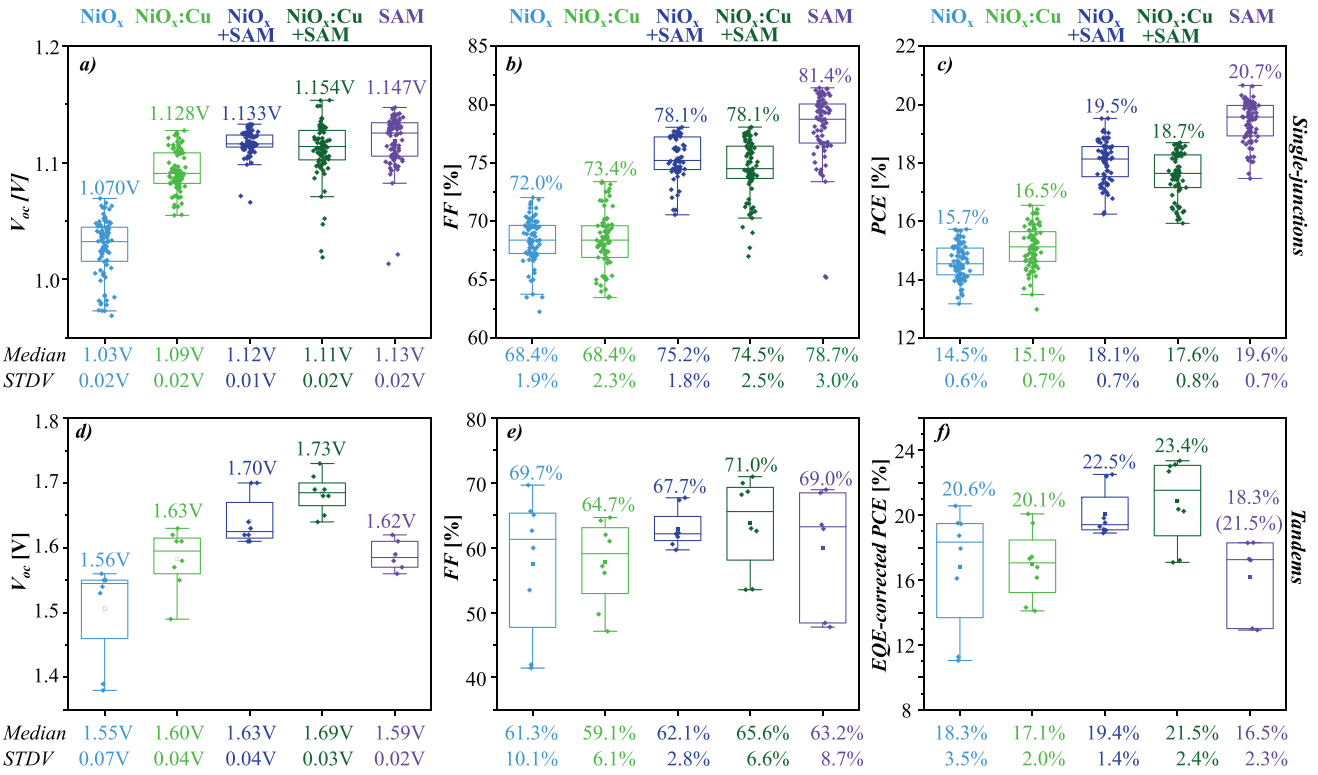

Figure 2. a,d) open-circuit voltage; b,e) fill factor; c,f) power-conversion efficiency of single-junction perovskite and CIGSe-perovskite monolithic tandem solar cells, respectively.

for the tandem devices, the most prominent changes are seen in the open-circuit voltage V_{oc}. Doping the NiO_x with 2% Cu is beneficial for the V_{oc} for both single-junction perovskite and CIGSe-perovskite tandem solar cells, with an average V_{oc} gain of around 60 and 70mV respectively (Figure 2a,d). In the single-junction solar cells, passivating the NiO_x or NiO_x:Cu with SAM improves the median value of the V_{oc} by 20–30mV compared to the cells with NiO_x:Cu as a stand-alone HTL. In addition, the SAM-passivated NiO_x and NiO_x:Cu yield almost identical V_{oc} to the devices with SAM as the stand-alone HTL. Therefore, for the single-junction solar cells, we conclude: 1) the SAM-surface passivation of the NiO_x:Cu does not yield as high V_{oc} gain as it does for the NiO_x and 2) we reach a V_{oc} saturation point already in some of the record devices with NiO_x:Cu as a stand-alone HTL. Nevertheless, despite the similar V_{oc}, the single-junction devices with SAM as a stand-alone HTL still outperform the NiO_x(:Cu)+SAM devices due to 4%-5% higher *FF* in its median value.

However, as seen in Figures 1d and 2d–f, the situation changes in the tandem devices, where SAM displays a drop in the V_{oc} and NiO_x:Cu+SAM becomes the most efficient HTL with V_{oc} of 1.7V, *FF* of 71% and *PCE* of 23.4%. The NiO_x's V_{oc} behaves similarly as it does in single-junction devices and it can be improved either by Cu doping or by SAM surface passivation. However, NiO_x:Cu as well as SAM display a different V_{oc} behavior in the tandem configuration as opposed to the single-junction configuration. More specifically, we see a prominent average gain in V_{oc} of around 100mV (from $V_{oc,\,average} = 1.58$ to $V_{oc,\,average} = 1.68V$) when we change from NiO_x:Cu to NiO_x:Cu+SAM as an HTL configuration in the tandem devices. The average V_{oc} of the SAM tandem devices (1.59V) is 50mV smaller than the average V_{oc} of the NiO_x+SAM tandem devices (1.64V) and 90mV smaller than the average V_{oc} of the NiO_x:Cu+SAM tandems (1.68V) tandems respectively.

Moving onto the *FF*, we point out that its analysis in monolithic tandems with current mismatching is not always straightforward. Literature points out that the lowest *FF* is achieved either at or close to the current-matching operation, while the maximum *FF* is achieved for mismatched cells.[86–89] Therefore, the *FF* in current-mismatched monolithic tandem solar cells, as is the case with the cells presented in this study, can often recoup the *PCE* losses caused by the J_{sc} losses from the current-limiting cell. With the exception of the CIGSe-perovskite tandem with MeO-2PACz, all tandems in this study are similarly mismatched, with a maximum J_{sc} mismatch between the two sub-cells of 1.1mA cm^{-2}. This means that the expected increase in the *FF* due to the current mismatching would be comparable across all samples and therefore, the trend in the *FF* as we move on from one HTL to the next would remain unchanged.

For the *FF* and *PCE*, we detect a similar trend for both the single-junction and the tandem devices. NiO_x and NiO_x:Cu yield almost statistically equal *FF* however, when comparing only these two HTL configurations, the champion *FF* of 73.4% in the single junctions is obtained with NiO_x:Cu, while in the tandems with NiO_x (70%). Combining the record *FF* and the record V_{oc}, we see a slightly superior *PCE* of the NiO_x:Cu (around 0.7% increase in the median *PCE* value) in the single-junction devices and of NiO_x (around 1.2% increase in the median *PCE* value) in the tandem devices. We also observe a 1mA cm^{-2} decline in the

J_{sc} in the single-junction solar cells caused by parasitic losses in the NiO_x:Cu films due to higher absorption (Supporting Information).

Moving onto the samples with SAM, on the one hand, we see slightly better *FF* and *PCE* in the NiO_x+SAM single-junction devices, as opposed to the devices with NiO_x:Cu+SAM as an HTL. On the other hand, for the tandem devices, the situation is reversed and - especially if we disregard the worst cell and consider it a statistical outlier - we obtain better *FF* and *PCE* for the tandems with NiO_x:Cu+SAM, than for the tandems with NiO_x+SAM, as an HTL.

The stand-alone SAM single-junction solar cells exhibit the highest *FF* and therefore *PCE*, but in the tandems, the champion *FF* of the SAM stand-alone devices is around 4% lower compared to the champion device with NiO_x:Cu+SAM. The remaining two devices with SAM show even more pronounced loss in the *FF*, eventually overlapping with the *FF* obtained with NiO_x(:Cu) as a stand-alone HTL. The *PCE* of the SAM devices is in the range of the *PCE* obtained with NiO_x or NiO_x:Cu, but one should keep in mind that the J_{sc} losses caused by the CIGSe bandgap change yield highly-underestimated *PCE*. Thus, for a hypothetical J_{sc} of around 19.5mA $cm^{-}2$ (as measured for the other devices), the SAM devices would have had around 3% higher *PCE* and a champion device with a *PCE* of around 21.5%. Nevertheless, the increase in the J_{sc} would have still not been enough to compensate for the losses in V_{oc} and the *FF* in the SAM-based devices, leaving NiO_x:Cu+SAM as the superior HTL.

The changes we detect in the V_{oc} across the different HTL configurations as well as we change from single-junction to tandem solar cells, open up several important questions. First, why does the V_{oc} in the single junctions have a different trend than in the tandems? Second, why is the SAM surface passivation beneficial for the V_{oc} obtained in the NiO_x-based solar cells (both in single junctions and tandems), but for NiO_x:Cu, the effect is much more pronounced in the tandems? Last, why does SAM not yield as high V_{oc} as NiO_x:Cu+SAM in the tandem devices, similarly to the way it does in the single-junction devices? We try to answer these questions in the following sections, first by analyzing the charge-carrier dynamics at the interfaces and then by performing X-ray and UV photoelectron spectroscopy (XPS and UPS) studies in order to discuss the reasons behind the devices' V_{oc} trends.

2.2. Charge-Carrier Dynamics at the HTL-Perovskite Interface: TrPL and tr-SPV Study

We now investigate the charge-carrier dynamics at the HTL-perovskite interfaces and dwell deeper into the physical reasons behind the changes we detect in the devices' V_{oc}. We do so by measuring transient surface photovoltage (tr-SPV)[90] and absolute and time-resolved photoluminesence (Tr)PL[91] of the perovskite films with varying HTLs (NiO_x, NiO_x:Cu, NiO_x + SAM, NiO_x:Cu + SAM or SAM) and substrate (ITO vs CIGSe), but without the presence of the electron-transport layers. With this approach, we probe only the impact of the HTL on the V_{oc}, but one should keep in mind that further limitations might be introduced by the ETL-perovskite interface as well.

We have decided to focus our discussion on the V_{oc} since out of all solar-cell parameters (V_{oc}, J_{sc}, *FF*, and *PCE*), the V_{oc} is the most suitable parameter for correlating the charge-carrier dynamics at the HTL-perovskite interface to the device performance. When we are performing the TrPL and tr-SPV measurements on the substrate + HTL + perovskite stacks, we are looking at the differences in the charge carrier dynamics only at the varied HTL-perovskite interface at open-circuit conditions. Therefore, our choice of characterization methods enables us to confidently correlate the charge-carrier dynamics and the V_{oc}, but since the *FF* and the V_{oc} are fundamentally interlinked to one another, the discussion on the V_{oc} with respect to the charge-carrier dynamics can be extended up to an extent to apply to the *FF* as well.

However, the *FF* and its reproducibility from one tandem to the next are not influenced only by the charge-carrier dynamics at the HTL-perovskite interface, but also by the above-discussed current mismatch or the formation of morphological defects and ohmic shunts, that might not necessarily affect the V_{oc}, but affect the *FF* and the formation of S-shaped *JV* curves.[84] Hysteresis can also have a larger impact on the *FF* than on the V_{oc}, but with the exception of two devices, our tandem solar cells do not exhibit strong hysteresis (refer to Supporting Information). Next, when we are looking at open-circuit conditions with the TrPL and tr-SPV measurements on the substrate + HTL + perovskite stacks, we are omitting the influence of the parallel and shunt resistances – both of which heavily affect the *FF*, but not necessarily the V_{oc}. The *FF* is also influenced by the dropping of the anti-solvent – varying distance to the sample and/or dropping the anti-solvent a second or two too late can influence the crystallization of the perovskite and the FF in the cells. Next, we also assume identical ideality factors across all bottom cells, identical surface roughness, absence of any lateral inhomogeneities, and identical micro- or macroscopic defects in both the bottom and the top devices. However, in reality, variations in these parameters are to be expected from one tandem to the next, explaining the increased statistical deviation in the median *FF* values compared to the statistical deviation in the median V_{oc} values in Figure 2.

Taking this into consideration, this work focuses exclusively on the charge-carrier dynamics at HTL-perovskite interface and how it affects the V_{oc} and the *FF* of both single-junction and tandem solar cells. By exploring the five HTLs on two different substrates and correlating their ten tr-SPV/TrPL measurements (**Figure 3**) to the devices' V_{oc}, we are providing a unique approach to systematically probe the HTL-perovskite interface. We investigate the charge-carrier extraction and recombination, and understand which performance-inhibiting processes are present at the HTL-perovskite interface. Finally, we also investigate whether the charge-carrier dynamics alters with respect to the substrate and show that when it comes to developing an HTL for tandem applications, the single-junction results might not be always directly transferable to the tandems. With respect to the tr-SPV signals, we consider three aspects. First, for the measurements performed at $f = 125kHz$, it is investigated if the signals are positive or negative. Positive tr-SPV signals indicate that the introduced HTL traps electrons, while negative tr-SPV signals can be induced by extracted free holes or hole trapping in the HTL. Second, it is considered when the signals reach their amplitude: the faster the tr-SPV maximum is reached, the faster the hole extraction is, which, in turn, should translate to a gain in the *FF* of the

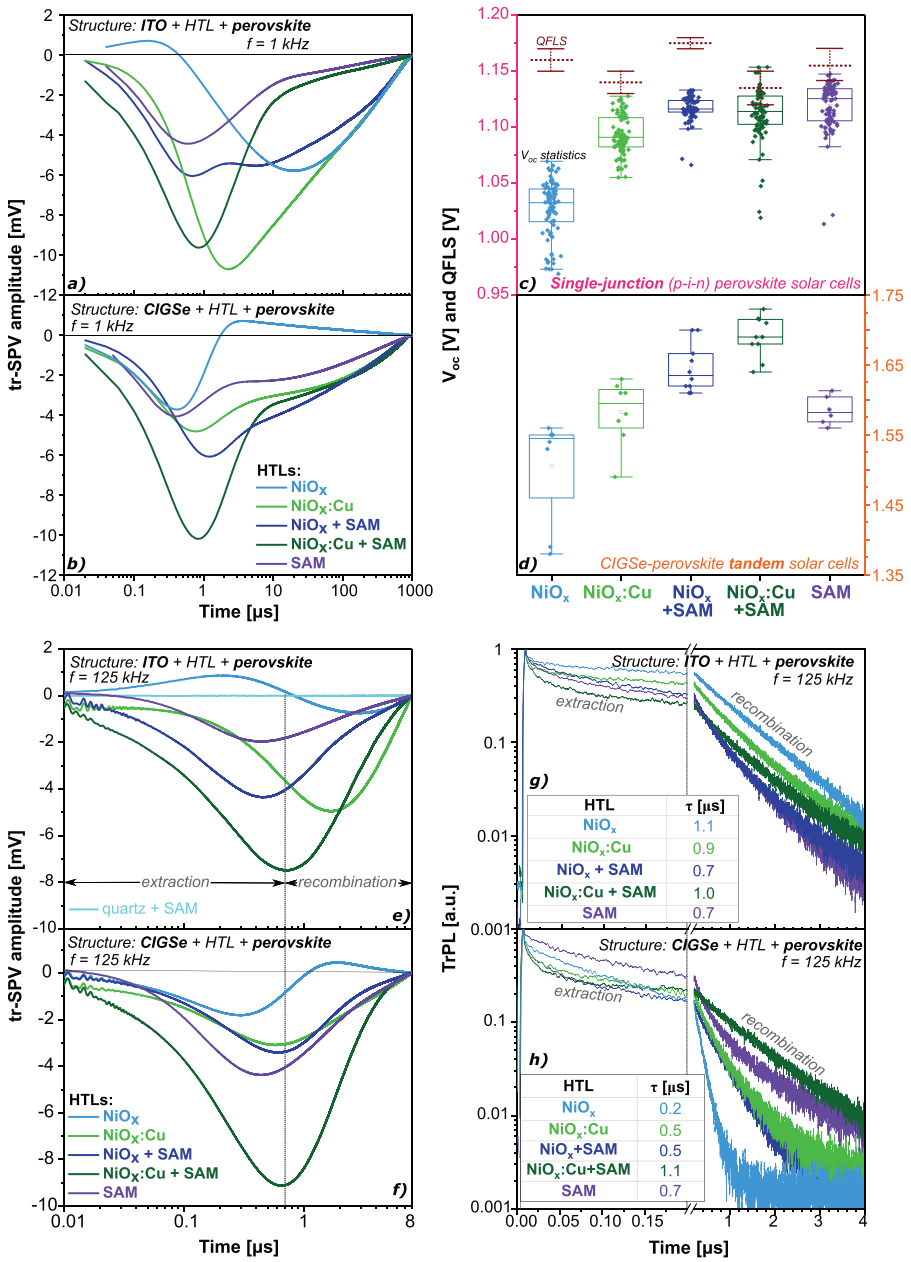

Figure 3. a,b) Tr-SPV measurements at $f = 1kHz$, c,d) V_{oc} and QFLS (only for *ITO* + HTL + perovskite, dashed line), e,f) tr-SPV measurements at $f = 125kHz$, and g,h) Tr-PL measurements at $f = 125kHz$ for single-junction perovskite (LHS) and CIGSe-perovskite monolithic tandem solar cells (RHS). The RHS is symmetrically mirrored to the LHS. The QFLS of the tandem configuration was not measured due to set-up limitations.

full device. Third, for the measurements performed at $f = 1kHz$, the tr-SPV amplitude, which can be influenced by charge-carrier recombination and serves as an indicator of where a higher V_{oc} can be expected, is analyzed and also fitted with a numerical model. In the simplest case, the higher the tr-SPV amplitude at $f = 1kHz$, the higher the V_{oc}. However, in these complex systems, with varying substrates and HTLs, as well as competing effects in the cells, considering only the tr-SPV amplitude as the main indicator for the device's V_{oc} could be misleading. Instead, it should be first identified whether electron trapping, delayed hole extraction, or both of these mechanisms limit the V_{oc} of the NiO_x devices, and then analyze how either the Cu-doping or the SAM passivation affect these V_{oc} inhibitors.

Next, we correlate the tr-SPV measurements to TrPL measurements performed at the same repetition rate ($f = 125kHz$) as the tr-SPV measurements. Combining the tr-SPV and the TrPL measurements allows us to distinguish between two possible reasons for a fast decay in the PL signal: 1) due to fast charge extraction,[92–94] or 2) due to electron trapping.[81] Finally, by performing an exponential-decay fit of the TrPL signals between

1 and 4 µs, we extract the effective PL lifetime of the carriers, which together with the quasi-Fermi level splitting can also provide insight into the dominant recombination processes in the solar cells.

The NiO_x:Cu+SAM HTL bi-layer yields the most straightforward results since it is not influenced by the change in substrate and displays very similar behavior in the tr-SPV and TrPL measurements for both the single-junction and the tandem configuration. We detect efficient charge carrier extraction, since the tr-SPV signals reach their amplitude in around 0.7µs (Figure 3e–f) and the TrPL signals show the steepest decay in the first 0.03 µs from all HTLs (Figure 3g–h). The continuous negative tr-SPV signals indicate there is no trapping of carriers, and the extracted effective PL lifetime is sufficiently large (around 1µs) for both single-junction and tandem configuration (Figure 3g–h). Finally, the quasi-Fermi level splitting (QFLS) extracted from the photoluminesence quantum yield (PLQY) points to a small QFLS-V_{oc} deficit in the single-junction solar cells (Figure 3c), indicating that the non-radiative recombination at the NiO_x:Cu+SAM-perovskite interface is not the dominant recombination mechanism.[95] This argument is further strengthened by the tr-SPV simulations presented in the next section, where we show that the concentration of interfacial traps, and not of non-radiative recombination defects (both surface and bulk), plays a crucial role in the performance of NiO_x:Cu as an HTL in the solar cells.

The partially-positive tr-SPV signals detected for NiO_x as a stand-alone HTL (Figure 3a,b,e,f) indicate that NiO_x exhibits pronounced trapping of electrons in both single-junction and tandem solar cells. Interestingly, in the single-junction solar cells, the trapping of the electrons (positive tr-SPV signals) occurs first, then the holes are poorly extracted (relatively slow evolution of the tr-SPV minima, low TrPL signal decay in the extraction-regime) and finally, the extracted carriers recombine slowly (relatively long tr-SPV decay and long TrPL-extracted effective time of 1.1µs).

In contrast, for the tandem solar cells with NiO_x as an HTL, the hole extraction occurs first, then the charge carriers recombine quickly (fast tr-SPV decay and fast TrPL decay with effective lifetime of ≈0.2µs, (Figure 3g–h), possibly due to the detected electron trapping at the later times (as indicated by the positive tr-SPV signals). The improved extraction compared to the single-junctions is not sufficiently strong to overcome the negative impact of the carriers trapping and the high recombination rate in the tandem configuration. Therefore, both the single-junction and the tandem devices with NiO_x exhibit unfavorable interfacial charge-carrier dynamics, yielding a significant QFLS-V_{oc} deficit in the single-junction and a low V_{oc} in both the single-junction and tandem devices (Figure 3c,d).

On the one hand, doping the NiO_x with Cu greatly improves the NiO_x in the single junctions, primarily because it completely cancels the charge trapping and then slightly speeds up the charge extraction (Figure 3a,b,e,f). On the other hand, passivating the NiO_x surface with SAM, improves the NiO_x in single-junction solar cells in a twofold manner: first, the incorporation of the SAM suppresses the charge trapping, similarly to the NiO_x:Cu, but in addition to this, it also enables a significantly faster charge-carrier extraction in the single-junction solar cells than the stand-alone NiO_x and NiO_x:Cu films (Figure 3a,b,e,f).

Comparing the extractions of the three HTLs (NiO_x, NiO_x:Cu and NiO_x + SAM), we see that in the single junctions the extraction regime and not the effective PL lifetime, is a better indicator of how high V_{oc} we can achieve in the devices. To be more precise, the effective lifetimes are comparable and they decrease only slightly from 1.1 to 0.9µs and finally to 0.7µs, but the charge extraction improves alongside with the average devices' V_{oc} from 1.03 to 1.09 and finally to 1.12V as we move from NiO_x, to NiO_x:Cu and finally to NiO_x + SAM, respectively. SAM as a stand-alone HTL in the single junctions displays very similar extraction (Figure 3e) and recombination regimes (Figure 3g) to the NiO_x + SAM. Thus, unsurprisingly, SAM and NiO_x + SAM yield similarly-performing single-junction perovskite solar cells, especially with respect to the V_{oc}.

However, the situation for NiO_x:Cu, NiO_x + SAM, and SAM in the tandems is not so straight-forward as in the single junctions. In the tandem devices, the HTL does not only enable the extraction/separation of the carriers as it does in the single-junctions, but also an effective recombination of the holes from the perovskite with the electrons from the CIGSe cell.[15] Therefore, analyzing the charge-carrier dynamics in the tandems is much more complex, since both the extraction and the recombination play a major role, but it is hard to quantify which one has a more pronounced effect as well as what happens when we slightly worsen one of these but significantly improve the other mechanism. This trade-off between the extraction and the effective lifetime is present in almost all samples, as we will continue to discuss throughout this section.

One of the most interesting findings is how differently the NiO_x:Cu behaves in the single-junction compared to the tandem configuration. First, the tr-SPV amplitude of the NiO_x:Cu at $f = 1kHz$ is significantly decreased as we move on from the tr-SPV measurement for single junctions (Figure 3a) to the measurements for tandems (Figure 3b). Connecting the amplitude suppression to the devices' V_{oc}, we see that in the single-junction solar cells, the NiO_x:Cu has a small QFLS-V_{oc} deficit. However, in the tandems, where the tandem's V_{oc} is the sum of the two subcells V_{oc}-s, we see non-negligible V_{oc} losses. Poor extraction is not very likely to be the cause for these losses since both tr-SPV and TrPL indicate a superior extraction of the NiO_x:Cu in the tandem compared to the single-junction devices. The decreased effective PL lifetime (from $\tau = 0.9$ to $\tau = 0.5$µs) in the tandems, which indicates faster recombination in the tandems compared to the single junctions, could partially explain why we detect V_{oc} losses in the tandems with NiO_x:Cu. However, the effective lifetime is not very likely to be the only reason for the worsened performance of the NiO_x:Cu, since NiO_x + SAM has the same effective lifetime as NiO_x:Cu, but statistically higher V_{oc}, while SAM yields higher effective lifetime (0.7µs), but the V_{oc} is in the same regime as NiO_x:Cu.

Looking at the tr-SPV measurement for NiO_x + SAM in the tandem configuration at $f = 125kHz$ (Figure 3f), it might seem like NiO_x + SAM has delayed extraction compared to NiO_x and just as fast extraction as NiO_x:Cu, since both NiO_x:Cu and NiO_x + SAM reach their maxima at the same time and later than NiO_x. However, looking more closely at the TrPL measurements, we see that NiO_x + SAM, with its fast-decaying signal, exhibits a significant improvement in the extraction compared to NiO_x and up to an extent, to NiO_x:Cu. In addition, the extraction regime of NiO_x

+ SAM actually improves when moving from a single-junction to a tandem configuration, as seen by the much faster decaying TrPL signal in the tandem (Figure 3h) than in the single-junction (Figure 3f) configuration. Comparing the recombination regimes of the NiO_x + SAM and NiO_x:Cu, we see that the effective PL lifetime of NiO_x + SAM decreases by around 30% (from 0.7 to 0.5µs) and of NiO_x:Cu by around 45% (from 0.9 to 0.5µs) as we move on from a single-junction to a tandem configuration (Figure 3f–h).

Moving onto the tr-SPV signal of SAM, one might expect that the extraction with SAM in the tandems is more efficient than the extraction of NiO_x + SAM since the tr-SPV signal reaches its minimum slightly faster than NiO_x + SAM (Figure 3f). However, the smaller amplitude of the SAM tr-SPV signals compared to the NiO_x + SAM tr-SPV signals at $f = 1kHz$ (Figure 3b) indicates that NiO_x + SAM would yield higher V_{oc} in the tandem solar cells. A closer look at the TrPL measurements indicates that SAM does not extract the charge-carriers as effectively as NiO_x + SAM (Figure 3h), explaining why SAM yields V_{oc} losses in the tandems, despite the equal effective PL lifetime of 0.7µs in the single-junction and tandem configuration (Figure 3g,h) and the slightly higher effective lifetime compared to NiO_x + SAM (0.5µs) and NiO_x:Cu (0.5µs).

Therefore, the loss in V_{oc} for SAM-based tandem devices is because the higher effective PL lifetime cannot compensate for the poor extraction. For the NiO_x + SAM, the efficient and improved charge extraction in the tandem devices compared to the single-junction devices, can compensate for the 30% loss in effective PL lifetime and yield relatively well-performing tandem devices. But, for the tandem devices with NiO_x:Cu the loss in the effective lifetime is 45% compared to the single-junction devices and despite the fast charge extraction detected in the TrPL measurements, NiO_x:Cu leads to non-negligible V_{oc} losses in the tandems.

In conclusion, we showed that NiO_x:Cu + SAM is the only HTL configuration that does not exhibit losses in the extraction or in the effective PL lifetime as we change from an ITO to a CIGSe substrate. The combined effect of efficient charge extraction and long effective PL lifetime with a QFLS equal to the single junction's V_{oc}, explains well why we obtain the statistically highest V_{oc} with NiO_x:Cu + SAM in the tandem devices. For the remaining four HTL configurations in the CIGSe-perovskite tandem solar cells we reveal non-optimal charge-carrier dynamics at the HTL-perovskite interface. SAM is the superior HTL for the single-junction solar cells and enables the highest *FF*, but its worsened extraction in the tandem solar cells limits the tandem's performance. NiO_x experiences significant V_{oc} losses due to poor extraction and charge trapping in the single-junction solar cells and additional fast recombination in the tandem solar cells. The V_{oc} can be improved by diminishing the charge trapping either by Cu doping or surface passivation with SAM, where the latter one also improves the poor charge extraction of the NiO_x. However, both NiO_x:Cu and NiO_x + SAM suffer a loss in the effective PL lifetime when implemented in the tandems, indicating that these HTLs induce unfavorable recombination in the tandem solar cells.

However, it remains an open question why NiO_x:Cu yields statistically lower V_{oc} compared to NiO_x + SAM, especially since both HTLs display almost identical behavior in the tr-SPV and TrPL measurements performed at $f = 125kHz$ (Figure 3f–h). Additionally, it is unclear why the tr-SPV amplitude of NiO_x:Cu at $f =$ $1kHz$ is noticeably suppressed and the V_{oc} losses are increased as we compare the single-junction (Figure 3a) to the tandem configuration (Figure 3b). We investigate these questions in the upcoming sections, first by simulating the tr-SPV results and second by performing XPS and UPS measurements.

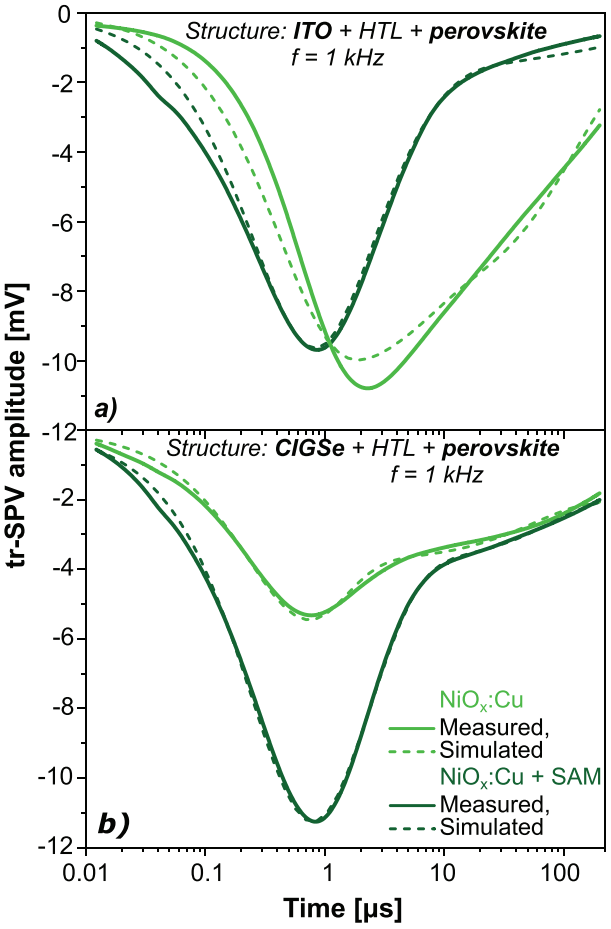

Figure 4. tr-SPV measurements at f = 1kHz (solid green lines) and tr-SPV simulations (dashed green lines) for a) single-junction configuration b) and tandem configuration either with NiO_x:Cu (light green) or NiO_x:Cu + SAM (dark green) as HTL.

2.3. tr-SPV Simulations

We fit the tr-SPV signals for NiO_x:Cu and NiO_x:Cu + SAM by using a simplified version of the kinetic model presented in [81]. *Equations* 1–5 in the Supplementary Information describe the simulation model we use here. When these five equations converge with *Equation* 6, which follows the experimental tr-SPV signal, we are able to extract information about carriers (re)injection, interface trap concentration, and non-radiative recombination defects concentration on the surface or in the bulk of the perovskite. The fit and the experimentally-measured tr-SPV signals are shown in **Figure 4** below, while the extracted parameters from the fitting are shown in **Table 1**.

Interestingly, NiO_x:Cu + SAM and NiO_x:Cu have a similar concentration of non-radiative defects in the single-junction and in

Table 1. Main fitting constants of the simulation: $N_{non-rad}$: concentration of non-radiative recombination defects (both surface or bulk); N_{int}: interface trap concentration; K_h or K_e: hole or electron injection rate, respectively; K_{hb} or K_{eb}: hole or electron reinjection rate, respectively. STD is the average standard deviation of the fit from the experimental SPV signal. The simulated fits for the single-junction configuration deviate more significantly from the experimental data compared to the tandem configuration due to a more pronounced asymmetry in the experimental signals.

Substrate	Interface	$N_{non-rad}$ $\times 10^{13}$ [cm^{-3}]	N_{int} $\times 10^{12}$ [cm^{-3}]	K_h $\times 10^5$ [s^{-1}]	K_e $\times 10^5$ [s^{-1}]	K_{hb} $\times 10^5$ [s^{-1}]	K_{eb} $\times 10^5$ [s^{-1}]	STD [%]
ITO	NiO_x:Cu	5	5	5	0.6	0.2	9	17
CIGSe	+ perovskite	7	20	5	0.5	8	6	7
ITO	NiO_x:Cu + SAM	6	8	10	2	2	0.5	14
CIGSe	+ perovskite	6	4	10	0.6	4	5	4

the tandem configuration ($N_{non-rad} = (6 \pm 1) \times 10^{13} cm^{-3}$), implying that SAM does not affect the rate of non-radiative recombination in the devices with NiO_x:Cu as an HTL. Moreover, since deep defects have been shown to act as non-radiative recombination centers that decrease the carrier density and the charge-carrier lifetime,[96] we can conclude that incorporating SAM on top of the NiO_x:Cu does not induce changes in the density of deep traps in the perovskite bulk compared to the case when NiO_x:Cu is used as a stand-alone HTL.

However, the tr-SPV simulations also reveal that NiO_x:Cu has a four times larger concentration of interface traps (N_{int}) in the tandem (20×10^{12}cm^{-3}) than in the single-junction ($5\times 10^{12} cm^{-3}$) configuration. The increased amount of interface/shallow traps can also explain why NiO_x:Cu yields half the effective PL lifetime in the tandem configuration compared to the NiO_x:Cu + SAM (0.5µs vs 1.1µs, Figure 3h). Therefore, SAM passivates the surface defects of the NiO_x:Cu, such as the commonly-known Ni^{2+}-vacancy defects in the NiO_x,[23] and improves the NiO_x:Cu in the tandems in a two-fold manner. First, it doubles the holes injection rate (K_h) of NiO_x:Cu from 5×10^5 to $10^6 s^{-1}$. Second, it decreases the concentration of interface traps of the NiO_x:Cu to a fifth in the tandem configuration, down to $4\times 10^{12} cm^{-3}$, consecutively enabling longer effective PL lifetime and higher V_{oc} in the tandem solar cells.

2.4. XPS and UPS Measurements

In this section, we perform XPS and UPS measurements and take a closer look into the chemical and electronic properties of the perovskite films deposited on two different substrates and five different HTLs (**Figure 5**). The goal of these XPS and UPS measurements is to gain insight into the chemical and electronic properties of the perovskite films, bring the UPS measurements in the context of band alignment, and discuss how the VBM/WF shifts could possibly influence the previously-discussed charge-carrier dynamics at the HTL-perovskite interface. For most of the samples, the charge-carrier dynamics already indicated sufficiently well why some HTLs were more favorable than others for the devices' performance. However, the differences in the charge-carrier dynamics of NiO_x + SAM and NiO_x:Cu were very subtle and not clear enough to explain why NiO_x:Cu does not yield as high V_{oc} in the tandems as NiO_x + SAM (Figure 3). The tr-SPV simulations indicated that NiO_x:Cu has a high concentration of interface defects in the tandem configuration, providing one possible explanation as to why its performance worsens in the tandem solar cells. The UPS measurements presented in this section will provide one additional explanation: NiO_x:Cu suffers from band misalignment in the tandem solar cells, which can be improved by the SAM surface passivation that induces energetic changes in the perovskite's bulk.

We first perform XPS measurements on the $Cs_{0.05}(MA_{0.17}FA_{0.83})_{0.95}Pb(I_{0.83}Br_{0.17})_3$ perovskite film and measure all of its relevant XPS core peaks of iodine, lead, bromide, nitrogen, and carbon (I 3d, Pb 4f, Br 3d, N 1s, and C 1s). The Cs peak is too noisy due to low (< 2%) concentration of cesium in the film. We then analyze whether altering the underlying HTL or substrate results in changes in the chemical composition or electronic properties of the perovskite surface. Such chemical changes would be present if we detect alterations in the shapes or relative intensities of the peaks, which upon fitting would result in different elemental contributions on the perovskite surface. On the other hand, if the shape of the peaks remains the same, but all peaks are shifted on the binding energy scale by the same value, then we are expecting respective electronic changes in the film. We can additionally test if such electronic changes are truly present by performing UPS measurements from which we will extract the perovskite's valence-band maximum (VBM) and work function (WF). Finally, we point out that although we

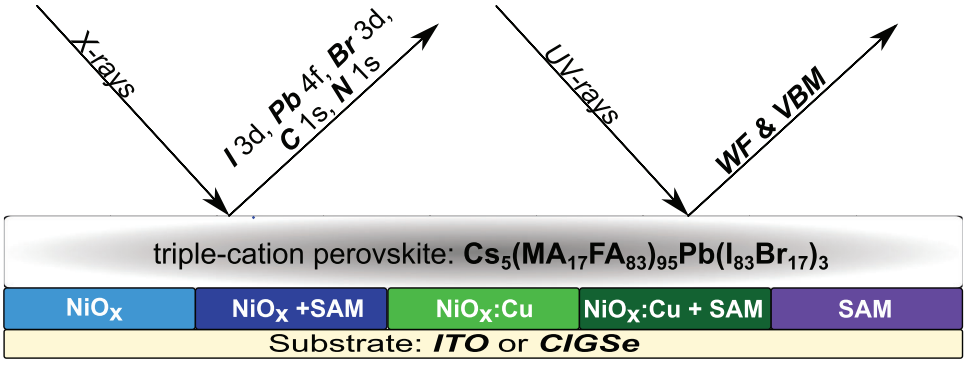

Figure 5. Sketch for the XPS and UPS measurements of the triple-cation perovskite film deposited on two substrates (ITO and CIGSe) and five HTLs (NiO_x, NiO_x + SAM, NiO_x:Cu, NiO_x:Cu + SAM, and SAM, where SAM is MeO-2PACz. This results in a total of ten XPS/UPS measurements.

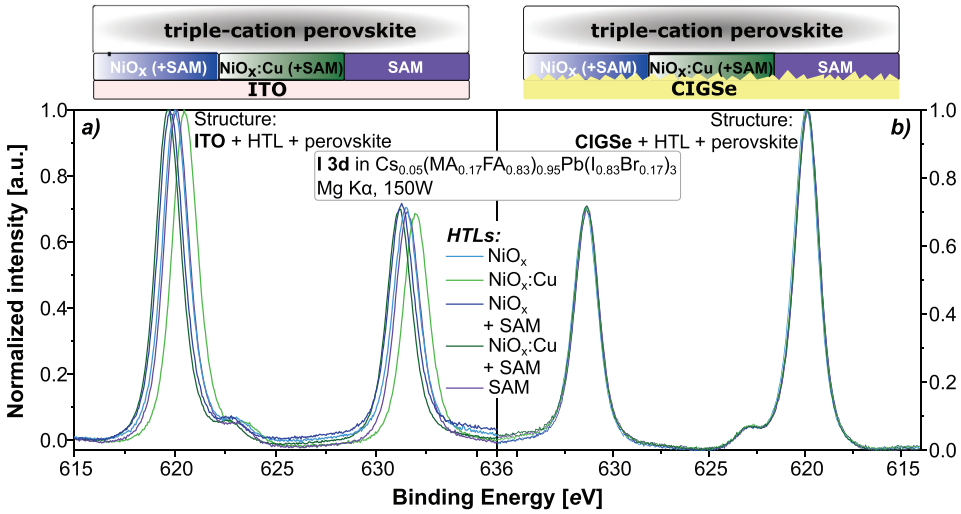

Figure 6. XPS Measurements: I 3d core peaks in triple-cation perovskite with varying HTLs below it and a) on an ITO as substrate or b) on a CIGSe solar cell as a substrate.

are measuring the perovskite surface, by altering the substrate or the HTL, we expect information about the entire stack—be it by diffusion of ions into the perovskite or by electronic changes that originate at the HTL-perovskite interface and then influence the perovskite surface, where we detect them.

In **Figure 6** below, we show the iodine 3d (I 3d) emission peak from the XPS measurements on the triple-cation perovskite film, while in **Table 2** we summarize the position of the main peaks and the full width at half maximum (FWHM) after fitting the I3d peak. The first and most prominent observation is that all XPS peaks exhibit much more noticeable shift when the different HTLs are deposited on ITO than on CIGSe. These shifts are similar for all detected photoemission peaks (as shown in Supporting Information).

The first reason why this shift could happen is if the sample was charging, for example due to a bad contact. This can happen during XPS measurements due to the X-ray induced emission of electrons from the sample, which need to be replenished in order to keep charge neutrality. If this is not the case, positive charging of the sample will lead to lower kinetic energies of the detected electrons, which translates into a higher binding energy. We exclude this as a reason since the measured resistance between the sample and the clamp with a multimeter indicated a satisfactory contact, as well as because the whole system is grounded in order to diminish charging effects.

The second reason could be a change of the surface chemistry. This option can also be excluded because a change in the surface chemistry would affect the different elements on the perovskite surface to a different extent, making a uniform shift both in magnitude and direction highly unlikely.

Another option is a light-induced surface photovoltage due to external light sources in the lab and in the measurement system. However, when the XPS measurements were repeated in darkness, the peak positions remained unchanged.

Therefore, we hypothesize that the reason for the less prominent shifts in the binding energy of all emission peaks for the CIGSe + HTL + perovskite compared to the ITO + HTL + perovskite configuration is due to the lower doping density of the CIGSe compared to the ITO. Different hole conductors with different dipole moments or trap concentrations lead to different concentrations of charges accumulated at the interface between perovskite and hole conductors. This behavior changes the bulk Fermi-level position in the mostly-intrinsic perovskite, leading to shifts in the binding energy of the I 3d emission peak when ITO is used as a substrate, where any X-ray induced excitation of carriers is quickly reversed by recombination due to the high doping density in ITO. However, when we have CIGSe in the back, the X-ray induced excitation of carriers in CIGSe leads to charge accumulation at the interface to the hole conductor. This happens because of the intrinsic electric field at the CIGSe/CdS interface and the low doping density in the CIGSe, leading to longer lifetimes of carriers. These charge carriers (electrons) now compensate the accumulated charges at the interface between perovskite and hole conductors, leading to no observable shifts in the XPS measurements.

In the case of the UPS measurements, which are characterized with a higher energy resolution and higher sensitivity to variations in the valence band maximum (VBM), the UV radiation is completely absorbed in the top-cell layers and does not

Table 2. Main peak position [eV] and full width at half maximum (FWHM) [eV] of I3d in triple-cation perovskite with varying hole-transporting layers and substrates below it.

HTL	Main Peak Position [eV]		FWHM [eV]	
	ITO	CIGSe	ITO	CIGSe
NiO_x	620.00	619.97	1.52	1.50
NiO_x:Cu	620.49	619.91	1.50	1.48
NiO_x + SAM	619.77	619.87	1.49	1.49
NiO_x:Cu + SAM	619.66	619.90	1.47	1.47
%hline SAM	620.08	619.87	1.47	1.48

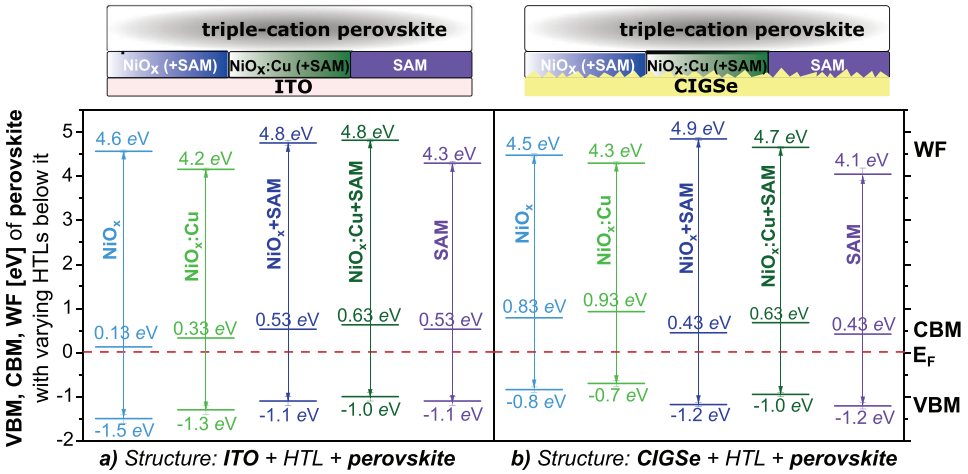

Figure 7. UPS Measurements: VBM, CBM and WF of triple-cation perovskite with varying HTLs below it (NiO_x (+SAM), NiO_x:Cu (+SAM), or SAM) a) on an ITO as substrate or b) on a CIGSe solar cell as a substrate.

even reach the CIGSe. Therefore, there is no compensation of charges since the UV radiation does not excite the CIGSe cell in the way that X-rays do. The UPS measurements then reveal true electronic changes within the perovskite film regardless of the substrate (ITO or CIGSe), resulting in a maximum measurable variation of 0.4eV in the valence band maximum (VBM) and 0.8eV in the work function (WF)(**Figure 7**a,b). These electronic changes can either lead to band banding or shifting of the Fermi level within the perovskite's bandgap. Fitting the I 3d core peak, exemplary for all emission peaks, and connecting the results with the VBM and WF changes (Figure 7), enable us to more carefully **1)** analyze the shifts in the perovskite films as we keep an HTL unchanged and change the substrate (e.g., from NiO_x:Cu on ITO to NiO_x:Cu on CIGSe); or, **2)** analyze the shifts in the perovskite as we change the HTL, but keep the substrate unchanged (for example, from NiO_x:Cu to NiO_x:Cu + SAM on ITO). Please note that due to simplicity, in the upcoming discussion we will only state the HTL, but the changes refer to the *perovskite film with this underlying HTL* and not to changes in the *HTL itself*.

2.4.1. Influence of the Substrate on the HTL-Perovskite Interface

We start by comparing the shifts in the binding energy of the I 3d peaks (Figure 6) to the changes in the UPS measurements (VBM and WF, Figure 7) as we deposit the HTL and the perovskite first on ITO and then on CIGSe. We find that the binding-energy shifts are in relatively good agreement with the shifts either in the VBM, in the WF, or in both (**Table 3**).

The only exception is NiO_x, which with a negligible 0.03eV shift in the binding energy of the I 3d peak does not correlate well to the 0.7eV and 0.1eV shifts in the VBM and the WF values, respectively. Moreover, the perovskite measured on ITO with NiO_x yields the biggest VBM offset of 1.5eV, indicating that NiO_x changes the nature of the perovskite film from an intrinsic to an n^{++} material. This prominent change could possibly result in an energetic barrier, preventing the efficient charge extraction and strengthening the charge trapping which we detected via the tr-SPV measurements.

Table 3. Comparison of the shift in the binding energies of the I 3d XPS peak positions ($\Delta BE = BE_{(ITO+HTL+pero)} - BE_{(CIGSe+HTL+pero)}$) to the shifts in the VBM ($\Delta VBM = VBM_{(ITO+HTL+pero)} - VBM_{(CIGSe+HTL+pero)}$) and the WF ($\Delta WF = WF_{(ITO+HTL+pero)} - WF_{(CIGSe+HTL+pero)}$) of the triple-cation perovskite as we change the substrate from ITO to CIGSe, but keep the HTL unchanged.

HTL	ΔBE [eV]	ΔVBM [eV]	ΔWF [eV]
NiO_x	0.03	0.7	0.1
NiO_x:Cu	0.58	0.6	–0.1
NiO_x + SAM	–0.1	–0.1	–0.1
NiO_x:Cu + SAM	–0.24	0	0.1
SAM	0.21	–0.1	0.2

NiO_x:Cu displays the most prominent shift in the I 3d binding energy as we switch from the ITO to the CIGSe substrate. The 0.58eV shift in the iodine's binding energy correlates well to a 0.6eV shift in the VBM of the perovskite deposited on top of NiO_x:Cu (Table 3). This pronounced shift is already an indication that there is a strong change in the band alignment of the NiO_x:Cu to the perovskite as we deposit it on CIGSe. The entanglement of the changes in the band alignment and the high interface trap concentration (Table 1) could explain why we detected a strong alteration in the tr-SPV signals and the devices V_{oc} (Figure 3).

Finally, depositing SAM on top of NiO_x(:Cu) yields an XPS shift to higher binding energy when changing from ITO to CIGSe substrate. Furthermore, all samples with SAM exhibit small XPS and UPS shifts in the range of 0.1 to 0.2eV that correlate well enough with each other, indicating that the SAM-perovskite interface is not as sensitive as the NiO_x(:Cu)-perovskite interface to a change in the substrate.

2.4.2. Influence of the HTL on the HTL-Perovskite Interface

For the perovskite films deposited on top of ITO + HTL (Figure 7a), we detect absolute VBM values between 1.0 and

1.5eV and WF values between 4.2 and 4.8eV. The bilayer of NiO_x(:Cu) + SAM yield the most-favorable WF of the perovskite film, with a value of 4.8eV, and a VBM of around 1.0–1.1eV, making these two measurements in relatively good agreement with other perovskite's WF and VBM values reported in literature.[5,97] The perovskite films deposited on SAM or NiO_x:Cu differ by 0.1 to 0.2eV in their WF and VBM values.

For the perovskite films deposited on top of CIGSe + HTL (Figure 7b), we detect VBM values between 0.8 and 1.2eV and WF values between 4.1 and 4.9eV. Unsurprisingly, NiO_x:Cu + SAM HTL bi-layer once again enables optimal VBM and WF values of the perovskite film. NiO_x + SAM enables the largest WF of 4.9eV, but a VBM of 1.2eV might not be optimal. NiO_x, NiO_x:Cu, and SAM as stand-alone HTLs in the tandems suffer from low WF (in the range of 4.1 to 4.5eV).

Next, we analyze more carefully the influence of SAM on the NiO_x(:Cu). Adding SAM on top of ITO + NiO_x:Cu (Figure 7a) results in an XPS shift to lower binding energy by 0.83eV, correlating excellently to a total 0.9eV shift in the UPS measurements: 0.3eV shift in the VBM and 0.6eV increase in the WF. Adding SAM on top of the ITO + NiO_x results in an XPS shift to lower binding energy by 0.23eV, which correlates well to a 0.2eV increase in the WF. However, the favorable 0.4eV shift in the VBM ($VBM_{NiO_x} = 1.5eV$ vs $VBM_{NiO_x+SAM} = 1.1eV$) remains undetected by the XPS measurements.

Nevertheless, these UPS measurements show that passivating the NiO_x(:Cu) surface with SAM enables favorable changes in the WF and in the VBM or the perovskite film.

The situation in the tandems is similar since passivating the NiO_x(:Cu) deposited on a CIGSe cell yields a favorable 0.4eV increase in the WF (Figure 7b). Interestingly though, SAM passivation of the NiO_x and of the NiO_x:Cu shifts the perovskite VBM further away from the Fermi level by 0.4 and 0.3eV, respectively. However, the 1.0eV VBM value of the perovskite on top of the NiO_x:Cu + SAM is more favorable than the 1.2eV VBM value obtained with NiO_x + SAM.

Therefore, in both the single-junction and tandem configuration we detect that passivating the NiO_x(:Cu) surface with SAM yields an increase in the perovskite's WF. Similar findings for the SAM passivation of ITO and the rise in the WF have been ascribed to a surface SAM-induced dipole moment.[72,73] Similarly, for NiO_x, passivation with a diethanolamine (DEA) self-assembled monolayer revealed that DEA enabled the formation of a dipole on the NiO_x surface and positively affected the NiO_x-perovskite interface by improving the perovskite's crystallinity, and by reducing the number of trap states and pinholes.[98] Additionally, as already discussed for the tr-SPV simulations, SAM passivates the NiO_x(:Cu) surface defects (oxygen or nickel vacancies) through chemical bonding and enables faster charge extraction at the NiO_x(:Cu)-perovskite interface.[74–76]

2.4.3. Band Alignment of NiO_x:Cu in Single-Junction Perovskite and Monolithic CIGSe-Perovskite Tandem Solar Cells

Finally, it remains to bring these UPS measurements in the context of band alignment. To better understand the influence of the perovskite's WF, but also why the NiO_x:Cu has worsened charge-carrier dynamics and V_{oc} losses in the tandem devices, we cross-compare the band alignment of the NiO_x:Cu in both single-junction and tandem solar cells. We find that when we deposit the NiO_x:Cu on CIGSe instead of ITO, the WF decreases from 4.8 to 4.5eV, while the VBM increases (in absolute value) from 0.74 to 0.97eV (see Supporting Information). Combining this data with the perovskite's UPS measurements on top of NiO_x:Cu (Figure 7a,b), enables us to present the respective band diagrams in **Figure 8** below. Figure 8a,b shows an electronic structure of ITO/AZO - NiO_x:Cu - perovskite aligned with respect to the vacuum and before they are brought into (an electrical) contact. In Figure 8c,d, we align the Fermi levels of the materials and discuss the band alignment (in the dark) upon electrical contact among the materials. We also note that the ITO Fermi level value was retrieved from Figure 4 in [23], while the band structure for AZO was retrieved from Figure 5 in [15].

As already discussed in the Introduction, the HTL in the tandems has two functions: enabling holes separation and extraction, and forming a recombination junction for an effective recombination of holes from the top with the electrons from the bottom cell. For these two processes to happen effectively, a favorable band alignment in the tandem solar cells is of paramount importance. Ideally, the VBM of the NiO_x:Cu should be *higher* than the VBM of the triple-cation perovskite; however, as seen in Figure 8d, the VBM of the NiO_x:Cu lies unfavorably lower than the VBM of the perovskite film. This is not the case in the single-junction configuration shown in Figure 8c, where the ITO - NiO_x:Cu - perovskite alignment yields better energetic compatibility. With respect to the AZO - NiO_x:Cu interface, we detect a CBM(AZO)- VBM(NiO_x:Cu) offset of 1.16eV, which yields an energetic barrier which the carriers cannot tunnel through.

Therefore, we can conclude that the V_{oc} losses of the NiO_x:Cu in the tandem compared to the single-junction devices are not caused only by an increase in the interface-traps concentration, but also by a poor band alignment with energetic barriers at the AZO-NiO_x:Cu and NiO_x:Cu-perovskite interfaces. However, passivating the NiO_x:Cu surface with SAM positively influences the overall band alignment, since depositing the perovskite on top of CIGSe + NiO_x:Cu + SAM results in a WF increase from 4.3 to 4.7eV and a VBM decrease from -0.7 to -1.0eV compared to depositing the perovskite on top of CIGSe + NiO_x:Cu (Figure 7). This means that the SAM passivation of the NiO_x:Cu pushes the HOMO of the perovskite from 5.0 to 5.7eV and therefore, improves the band alignment with respect to the NiO_x:Cu since the VBM of the NiO_x:Cu + SAM would then lay above the perovskite's HOMO. In other words, NiO_x:Cu + SAM becomes the most efficient HTL in the tandem solar cells because NiO_x:Cu acts as a shunt-quenching layer below the SAM, while the SAM suppresses the NiO_x's surface traps and improves the NiO_x's band alignment to the AZO and the perovskite film.

3. Conclusion

In conclusion, our work analyzed the charge-carrier dynamics at the HTL-perovskite interface in order to understand its main limitations and consecutively, optimize the HTL for monolithic CIGSe-perovskite tandem solar cells. We investigated the performance of five HTLs (NiO_x, NiO_x:Cu, NiO_x + SAM, NiO_x:Cu + SAM, and SAM as a stand alone HTL) in a step-wise manner and systematically analyzed the influence of the NiO_x's doping

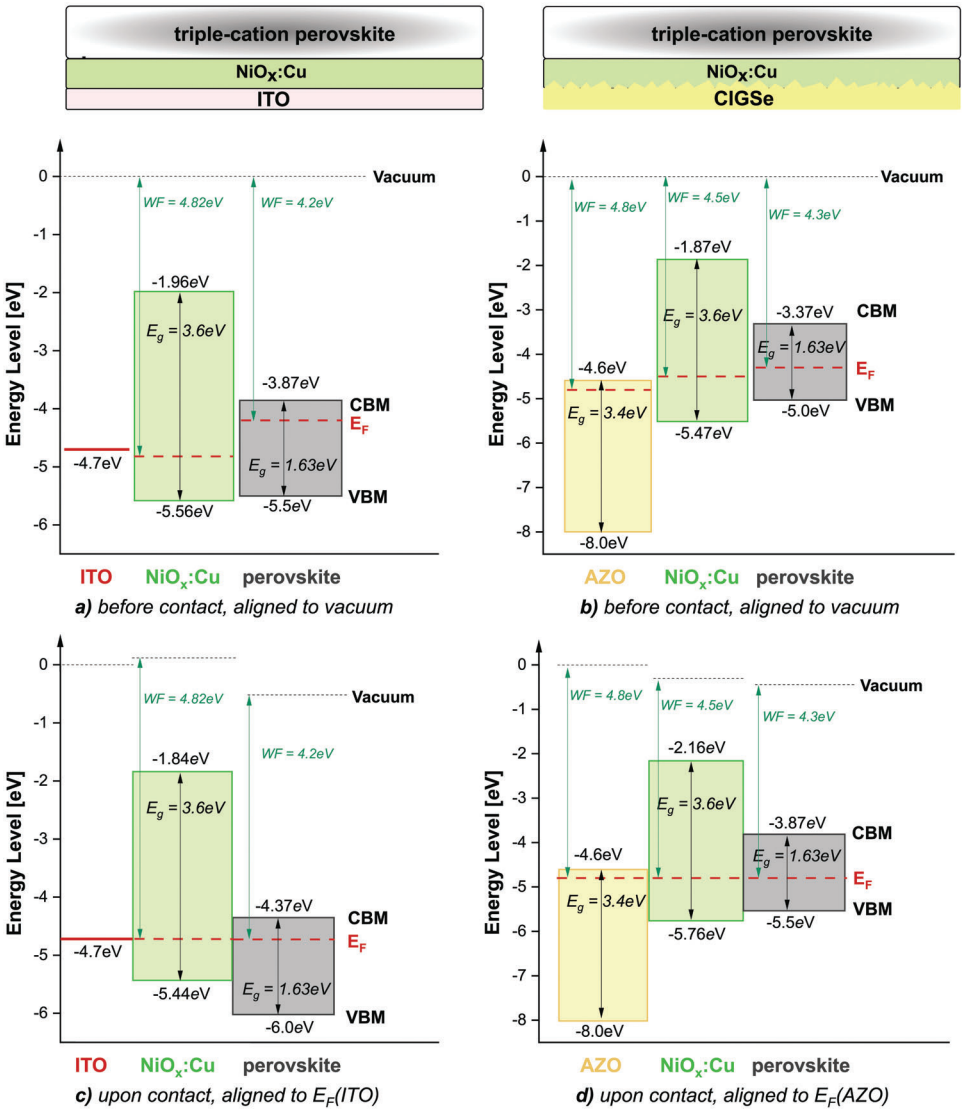

Figure 8. Band alignment of NiO_x:Cu to ITO (LHS, for single-junction configuration) or AZO (RHS, for tandem configuration) and triple-cation perovskite. Subfigures a,b): alignment to vacuum level, situation before the three materials are brought into electrical contact; c,d): alignment to the Fermi level of ITO/AZO, situation without illumination after the three materials are brought into electrical contact.

and/or surface passivation on the overall device performance. We then correlated the solar-cells performance of the *p-i-n* single-junction perovskite and monolithic CIGSe-perovskite solar cells to tr-SPV, TrPL, XPS, and UPS measurements, as well as tr-SPV simulations, performed on a substrate + HTL + perovskite configuration (substrate: either ITO or CIGSe).

NiO_x:Cu + SAM is the most appropriate HTL for the tandem devices, predominantly due to its satisfactory hole-extraction rate, effective PL lifetime, and smaller amount of non-radiative recombination compared to NiO_x:Cu. SAM passivates the NiO_x:Cu surface defects and enables faster hole extraction and significant suppression of the interface-traps concentration. NiO_x:Cu + SAM also yields an increase in the perovskite's WF compared to NiO_x:Cu, most likely due to the effect of the SAM-induced diplole at the interface, enabling an overall better band alignment in the tandem devices. All of these advancements at the NiO_x:Cu + SAM-perovskite interface resulted in a monolithic CIGSe-perovskite tandems with a champion 1.7V V_{oc}, 71% *FF*, and 23.4% *PCE*. In addition to this high efficiency, to the best of our knowledge, this work is also the first successful demonstration of low-temperature sputtered NiO_x:Cu in the monolithic CIGSe-perovskite tandem solar cells.

The remaining four HTLs were found to be sub-optimal for CIGSe-perovskite tandem applications. NiO_x suffers from severe interfacial electron trapping, poor extraction of holes, and significant QFLS-V_{oc} deficit. The electron trapping can be suppressed either by Cu doping or by SAM passivation, where the latter also provides faster extraction of the holes. However, in the tandems, NiO_x:Cu suffers from more pronounced V_{oc} losses than in the single-junction devices, primarily due to a prominent increase in the interface-traps concentration in the tandem compared to the single-junction configuration with NiO_x:Cu.

The different NiO_x:Cu behavior in the single-junction and in the tandem solar cells demonstrates that optimizing an HTL for single-junction solar cells might not always be the best approach if one wants to transfer the HTL to a tandem device, since the changes at the HTL-perovskite interface caused by the change in the underlying substrate will affect the whole tandem device.

Finally, we point out that we correlate the charge-carrier dynamics at the HTL-perovskite interface and the chemical and electronic changes on the perovskite surface to the performance of the finished devices, but the electron-transport layers (ETLs) that are placed on top of the perovskite in the finished devices will induce electronic changes in the entire stack once again. Therefore, in order to go beyond the current world-record monolithic CIGSe-perovskite tandem devices, future work should also focus on understanding and surpassing the limitations of the ETL-perovskite interface.

4. Experimental Section

Samples Preparation: For the single-junction solar cells, pattered ITO subjected to 15 min ultrasonic cleaning with soap, DI water, acetone, and isopropanol was used. The cleaning procedure was finalized with a 15 min UV-O_3 cleaning. The CIGSe bottom solar cells were manufactured via a co-evaporation process[99] and with a RbF post-deposition treatment.[100] The 60nm-thick CdS layer was deposited by dipping the samples into a 60°C heated solution of DI water and Cd-acetate (2.5 mM, purity >98%), thiourea (0.05 M, purity >99%) and aqueous ammonia solution (max. contamination ⩽260ppm, the ammonia was GPR RECTAPUR) until the CdS grows via the reactions described in [101]. The intrinsic (i-ZO, 40nm), and the aluminum-doped (AZO, 60nm) zinc oxide were deposited via radio-frequency (RF) sputtering. The active area was defined with a P1 laser scribe on the tandem surface in order to prevent current leakage in the finished tandem devices. Unlike the ITO, the CIGSe solar cells were not subjected to wet-chemical cleaning prior to the deposition of the HTL.

NiO_x (15nm - 20nm) was deposited via a low-temperature, in-vacuum RF sputtering process from a NiO_x (99.9% purity, Nova Fabrica) or NiO_x:Cu target (2%Cu, Nova Fabrica) in pure Ar (99.999%) atmosphere, at a power of 60W, pressure of $(4.7 \pm 0.1) \times 10^{-3}$ mbar, and ≈ 5cm target-to sample distance. The sputtering bias was constant during sputtering. The samples were not annealed post-sputtering, since high temperatures can cause a diffusion of the Cd from the CdS buffer layer into the CIGSe absorber and destroy the cell's performance. Post-sputtering, the samples were transferred to and sealed in a N_2-filled glovebox. The samples with NiO_x(:Cu) as a stand-alone HTL were then opened in another N_2-filled glovebox for the perovskite deposition.

The samples that were subjected to SAM deposition, underwent 15 min O_3 treatment in a UV-O_3 cleaner before the SAM deposition. The UV light was blocked by putting a glass cover on top of the samples. The SAM used throughout this work was the MeO-2PACz ([2-(3,6-dimethoxy-9H-carbazol-9-yl) ethyl]phosphonic acid) self-assembled monolayer. 100µl of 1mM SAM solution (MeO-2PACz powder >98% purity (TCI) dissolved in anhydrous ethanol (VWR chemical)) were spin-coated at 4000 rps for 45 s, after which the samples were annealed at 100°C for 10 min. The samples were then transferred through N_2 for the perovskite spin-coating.

In order to truly understand only the influence of the HTL on the overall device performance and decouple it from other influences in the cell, we investigate only one perovskite configuration throughout the work: $Cs_{0.05}(MA_{0.17}FA_{0.83})_{0.95}Pb(I_{0.83}Br_{0.17})_3$ (CsMAFA), E_g = 1.63eV.[102] PbI_2 and $PbBr_2$ salts (both with 99.99% purity, TCI manufacturer) were mixed with a 4:1 ratio DMF:DMSO mixture (DMF: N,N-dimethylformamide, DMSO: dimethylsulfoxid, Sigma-Aldrich manufacturer). The solutions were then shaked overnight at 60°C. The following day, FAI salt (formamidinium iodide, 99.99% purity, dyenamo manufacturer) was mixed with a cooled PbI_2 solution, yielding a $FAPbI_3$ (formamidinium lead iodide) solution. Similarly, MABr (methylammonium bromide, 99.99% purity, dyenamo manufacturer) salt was mixed with the cooled $PbBr_2$ solution, yielding a $MAPbBr_3$ (methylammonium lead bromide) solution. The CsI solution was prepared by dissolving CsI salt (cesium iodide, 99.999% Cs) in DMSO and without overnight shaking or heating. The final perovskite solution was obtained by mixing three solutions: $FAPbI_3$, $MAPbBr_3$, and CsI into one solution with the ratios presented in [102].

100µl of the perovskite solution were spin-coated at 4000 rpm for 40 s (out of which 5s were acceleration). 500µl of ethyl acetate (anhydrous, 99.8% purity, Sigma Aldrich manufacturer) were dropped as an anti-solvent 25 s after the start of the spin-coating. The perovskite films deposited on top of the ITO + HTL configuration and the CIGSe + HTL configuration were annealed at 100°C for an hour and half an hour after the spin-coating, respectively. Next, 23nm and 20nm of C_{60} was evaporated on the single-junction and on the tandem devices, respectively. Afterward, the tandem devices receive a 20nm ALD-deposited SnO_2 at 80°C, 100nm sputtered IZO, twice a 100nm Ag-ring evaporation to define the 1.08cm^2 area of the tandem device, and finally 100nm LiF evaporation to provide an anti-reflective coating. Opposed to the tandem devices, after the C_{60} evaporation, the single-junction devices receive an 8 and 100nm of evaporated BCP layer and Cu grid, respectively.

Characterization Techniques: The *current density-voltage (JV) measurements* of the tandem devices were performed in air with a 12 LED sun simulator (Wavelabs manufacturer, class AAA). The calibration was done with a KG3 silicon reference cell and the samples were kept at temperature of 25°C throughout all of the measurements. The single-junction JV measurements were performed in a N_2 glove box using an Oriel class ABB sun simulator under a simulated illumination of an AM 1.5G spectrum. Each single-junction and tandem solar cell was measured without previous light-soaking or biasing in both a forward-bias ($V_{start} < V_{end}$) and in reverse-bias ($V_{start} > V_{end}$) scan direction.

The *external quantum efficiency (EQE) measurements* were performed with a home-built three-LED (blue, red, green) set-up, in a 300–770nm and 500–1250nm wavelength range for the perovskite and the CIGSe cell, respectively. The reflection (R) was measured by performing small-spot reflection measurements with a PerkinElmer Lambda 1050 dual-beam photometer with an integrating sphere in the spectral range from 300 to 1250nm. Both the EQE and the R measurements were performed with a 10nm wavelength step.

For the *transient surface photovoltage (tr-SPV)* and *time-resolved photoluminescence (TrPL) measurements*, we deposit the five HTLs either on ITO substrate or on a CIGSe cell, identical to the one used in the CIGSe-perovskite tandems devices. We then spin-coat the perovskite on top of the HTL in an identical manner as explained above, but omit the top electron layers since they can strongly influence both measurements.

The TrPL measurements were performed with a 660nm pulsed laser diode with an excitation spot diameter of ≈110µm and an averaged intensity of 100nW. The emitted photoluminescence was selected by a 700nm long-pass filter and the time-correlated single-photon counting technique enabled a signal recording for around 4µs. The injected carrier concentration (averaged over the perovskite absorber thickness of ≈500nm) was ≈$10^{15}cm^{-3}$ per laser pulse for a TrPL repetition rate of 125 kHz. This corresponds to ≈ 1 sun condition. More information on the set-up can be found in [91].

The tr-SPV measurements were performed with a pulsed 515nm excitation laser light with a 5mm spot size. The photo-excitation was done from the perovskite side. The repetition rate of the excitation pulse was either 1kHz or 125 kHz, where the latter was correlated to the TrPL measurements. The 125 and 1kHz measurements yield signals up to 8 and 1000µs, respectively. The fluence was controlled with neutral density filters and monitored with a power meter. The SPV signal was measured in the configuration of a parallel plate capacitor, consisting of a quartz cylinder partially coated with the SnO_2:F electrode and mica sheet as an insulator. Same as for the TrPL measurements, the injected carrier concentration (averaged over a perovskite thickness of ≈500nm) was ≈1015cm^{-3} per laser pulse for the tr-SPV measurements at 125 kHz. More information on the tr-SPV set-up can be found in [81, 90].

The *X-ray photoemission spectroscopy (XPS)* and the *ultraviolet photoemission spectroscopy (UPS)* were performed on the same ten stacks (two substrates and five HTLs) as the tr-SPV and TrPL measurements. We point out, however, that the XPS/UPS measurements were not performed on the *same samples* on which the tr-SPV/TrPL measurements were done. Since XPS and UPS were extremely sensitive to surface contamination, we perform air-free transfer of the perovskite films from the N_2-filled glove box where they were prepared to the in-vacuum XPS/UPS system. Thus, we ensure that the XPS core peaks as well as the WF/VBM were not influenced by contamination or varying air humidity. For the XPS measurements, we use an XR-50 X-ray source from SPECS with a Mg Kα anode (1253.6eV) at a power of 150W and a CLAM 4 electron analyser from VG at a pass energy of 20eV. For the UPS measurements we use an UV HeI (21.2eV) source and a 2.5eV pass energy. For details on the XPS/UPS setup, refer to [103]. The errors of the XPS and UPS measurements were obtained from the fitting procedures.

The *atomic force microscopy (AFM)* pictures/3D maps show the samples surface morphology of a representative 20 by 20 µm area. They were recorded using a XE-70 SPM with a silicon tip (PPP-NCHR) in dynamic mode. The raw data was visualized with the free software Gwyddion.

The *scanning electron microscope (SEM)* was a Zeiss Merlin FE-SEM. The SEM images were made with different magnificaions (can be read from under the SEM images in Supporting Information) and at accelerating voltages of 5k*e*V.

Supporting Information

Supporting Information is available from the Wiley Online Library or from the author.

Acknowledgements

The funding for this work was provided by the Federal Ministry of Education and Research (BMBF) through the project PEROWIN (grant no. 03SF0631) and by the Helmholtz Association within the projects HySPRINT Innovation lab, the EU Partnering project TAPAS and the project "Zeitenwende – Tandem Solarzellen", and by the Federal Ministry of Economoy and Energy (Bundesministerium für Wirtschaft und Energie) for the speedCIGS project (grant no. 0324095D). I.L. thanks the AiF project (ZIM-KK5085302DF0) for financial support. Artem Musiienko acknowledges a financial support from the German Science Foundation (DFG) in the framwork of the priority program SPP 2196 and Horizon Europe Framework Programm call (HORIZON-MSCA-2021-PF-01; acronym HyPerGreen; agreement number 101061809). The authors further acknowledge HyPerCells - a joint graduate school of the University of Potsdam and the Helmholtz-Zentrum Berlin, as well as T. Hänel, B. Bunn, J. Lauche, T. Münchenberg, E. Waack, R. Haberecht, A. Steigert, K. Mayer-Stillrich, M. Hartig, M. Kirsch, N. El-Ganainy, and M. Wittig for technical support during device fabrication, H. Hempel for the TrPL measurements, F. Ruske for the SEM images provided in Supporting Information, and D. Menzel for helpful discussion on the results.

Open access funding enabled and organized by Projekt DEAL.

Conflict of Interest

The authors declare no conflict of interest.

Data Availability Statement

The data that support the findings of this study are available from the corresponding author upon reasonable request.

Keywords

hole-transporting layers, monolithic CIGSe-perovskite tandem solar cells, NiO_x, photoemission spectroscopy, photoluminesence, self-assembled monolayers, surface photovoltage

Received: March 31, 2023
Revised: April 6, 2023
Published online: May 25, 2023

[1] Best Research-Cell Efficiency Chart, https://www.nrel.gov/pv/cell-efficiency.html.
[2] N. J. Jeon, J. H. Noh, W. S. Yang, Y. C. Kim, S. Ryu, J. Seo, S. I. Seok, *Nature* **2015**, *517*, 476.
[3] W.-J. Yin, T. Shi, Y. Yan, *Appl. Phys. Lett.* **2014**, *104*, 063903.
[4] K. X. Steirer, P. Schulz, G. Teeter, V. Stevanovic, M. Yang, K. Zhu, J. J. Berry, *ACS Energy Lett.* **2016**, *1*, 360.
[5] A. Al-Ashouri, A. Magomedov, M. Roß, M. Jošt, M. Talaikis, G. Chistiakova, T. Bertram, J. A. Márquez, E. Köhnen, E. Kasparavičius, S. Levcenco, L. Gil-Escrig, C. J. Hages, R. Schlatmann, B. Rech, T. Malinauskas, T. Unold, C. A. Kaufmann, L. Korte, G. Niaura, V. Getautis, S. Albrecht, *Energy Environ. Sci.* **2019**, *12*, 3356.
[6] A. Al-Ashouri, E. Köhnen, B. Li, A. Magomedov, H. Hempel, P. Caprioglio, J. A. Márquez, A. B. Morales Vilches, E. Kasparavicius, J. A. Smith, N. Phung, D. Menzel, M. Grischek, L. Kegelmann, D. Skroblin, C. Gollwitzer, T. Malinauskas, M. Jošt, G. Matič, B. Rech, R. Schlatmann, M. Topič, L. Korte, A. Abate, B. Stannowski, D. Neher, M. Stolterfoht, T. Unold, V. Getautis, S. Albrecht, *Science* **2020**, *370*, 1300.
[7] W. Shockley, H. J. Queisser, *J. Appl. Phys.* **1961**, *32*, 510.
[8] M. Jošt, E. Köhnen, A. Al-Ashouri, T. Bertram, Š. Tomšič, A. Magomedov, E. Kasparavicius, T. Kodalle, B. Lipovšek, V. Getautis, R. Schlatmann, C. A. Kaufmann, S. Albrecht, M. Topič, *ACS Energy Lett.* **2022**, *7*, 1298.
[9] J. Ramanujam, U. P. Singh, *Energy Environ. Sci.* **2017**, *10*, 1306.
[10] D. Kim, S. S. Shin, S. M. Lee, J.-S. Cho, J. H. Yun, H. S. Lee, J. H. Park, *Adv. Funct. Mater.* **2020**, *30*, 2001775.
[11] R. Caballero, C. A. Kaufmann, T. Eisenbarth, T. Unold, R. Klenk, H.-W. Schock, *Prog. Photovoltaics* **2011**, *19*, 547.
[12] M. A. Ruiz-Preciado, F. Gota, P. Fassl, I. M. Hossain, R. Singh, F. Laufer, F. Schackmar, T. Feeney, A. Farag, I. Allegro, H. Hu, S. Gharibzadeh, B. A. Nejand, V. S. Gevaerts, M. Simor, P. J. Bolt, U. W. Paetzold, *ACS Energy Lett.* **2022**, *7*, 2273.
[13] M. Nakamura, K. Yamaguchi, Y. Kimoto, Y. Yasaki, T. Kato, H. Sugimoto, *IEEE J. Photovoltaics* **2019**, *9*, 1863.
[14] Q. Han, Y.-T. Hsieh, L. Meng, J.-L. Wu, P. Sun, E.-P. Yao, S.-Y. Chang, S.-H. Bae, T. Kato, V. Bermudez, Y. Yang, *Science* **2018**, *361*, 904.
[15] Y. Wang, R. Wenisch, R. Schlatmann, I. Lauermann, *Adv. Energy Mater.* **2018**, *8*, 1801692.
[16] T. Ozturk, E. Akman, B. Surucu, H. Dursun, V. Ozkaya, S. Akin, *Eur. J. Inorg. Chem.* **2021**, *2021*, 4251.
[17] F. Wang, Y. Cao, C. Chen, Q. Chen, X. Wu, X. Li, T. Qin, W. Huang, *Adv. Funct. Mater.* **2018**, *28*, 1803753.
[18] T. Todorov, T. Gershon, O. Gunawan, Y. S. Lee, C. Sturdevant, L.-Y. Chang, S. Guha, *Adv. Energy Mater.* **2015**, *5*, 1500799.
[19] M. Jošt, T. Bertram, D. Koushik, J. A. Marquez, M. A. Verheijen, M. D. Heinemann, E. Köhnen, A. Al-Ashouri, S. Braunger, F. Lang, B. Rech, T. Unold, M. Creatore, I. Lauermann, C. A. Kaufmann, R. Schlatmann, S. Albrecht, *ACS Energy Lett.* **2019**, *4*, 583.
[20] A. Magomedov, A. Al-Ashouri, E. Kasparavičius, S. Strazdaite, G. Niaura, M. Jošt, T. Malinauskas, S. Albrecht, V. Getautis, *Adv. Energy Mater.* **2018**, *8*, 1801892.

[21] X. Guo, G. Luo, J. Liu, C. Liao, G. Wang, S. Li, *IEEE J. Photovoltaics* **2018**, *8*, 1039.
[22] H. Zhang, J. Cheng, F. Lin, H. He, J. Mao, K. S. Wong, A. K.-Y. Jen, W. C. H. Choy, *ACS Nano* **2016**, *10*, 1503.
[23] D. Di Girolamo, F. Di Giacomo, F. Matteocci, A. G. Marrani, D. Dini, A. Abate, *Chem. Sci.* **2020**, *11*, 7746.
[24] G. Li, Y. Jiang, S. Deng, A. Tam, P. Xu, M. Wong, H.-S. Kwok, *Adv. Sci.* **2017**, *4*, 1700463.
[25] E. Aydin, J. Troughton, M. De Bastiani, E. Ugur, M. Sajjad, A. Alzahrani, M. Neophytou, U. Schwingenschlögl, F. Laquai, D. Baran, S. De Wolf, *ACS Appl. Energy Mater.* **2018**, *1*, 6227.
[26] S. Pang, C. Zhang, H. Dong, D. Chen, W. Zhu, H. Xi, J. Chang, Z. Lin, J. Zhang, Y. Hao, *ACS Appl. Energy Mater.* **2019**, *2*, 4700.
[27] T. Abzieher, S. Moghadamzadeh, F. Schackmar, H. Eggers, F. Sutterlüti, A. Farooq, D. Kojda, K. Habicht, R. Schmager, A. Mertens, R. Azmi, L. Klohr, J. A. Schwenzer, M. Hetterich, U. Lemmer, B. S. Richards, M. Powalla, U. W. Paetzold, *Adv. Energy Mater.* **2019**, *9*, 1970035.
[28] B. Zhao, L. C. Lee, L. Yang, A. J. Pearson, H. Lu, X.-J. She, L. Cui, K. H. L. Zhang, R. L. Z. Hoye, A. Karani, P. Xu, A. Sadhanala, N. C. Greenham, R. H. Friend, J. L. MacManus-Driscoll, D. Di, *ACS Appl. Mater. Interfaces* **2018**, *10*, 41849.
[29] D. Koushik, M. Jošt, A. Dučinskas, C. Burgess, V. Zardetto, C. Weijtens, M. A. Verheijen, W. M. M. Kessels, S. Albrecht, M. Creatore, *J. Mater. Chem. C* **2019**, *7*, 12532.
[30] T. J. Jacobsson, A. Hultqvist, S. Svanström, L. Riekehr, U. B. Cappel, E. Unger, H. Rensmo, E. M. J. Johansson, M. Edoff, G. Boschloo, *Solar Energy* **2020**, *207*, 270.
[31] M. B. Islam, M. Yanagida, Y. Shirai, Y. Nabetani, K. Miyano, *ACS Omega* **2017**, *2*, 2291.
[32] Y. Hou, E. Aydin, M. De Bastiani, C. Xiao, F. H. Isikgor, D.-J. Xue, B. Chen, H. Chen, B. Bahrami, A. H. Chowdhury, A. Johnston, S.-W. Baek, Z. Huang, M. Wei, Y. Dong, J. Troughton, R. Jalmood, A. J. Mirabelli, T. G. Allen, E. Van Kerschaver, M. I. Saidaminov, D. Baran, Q. Qiao, K. Zhu, S. De Wolf, E. H. Sargent, *Science* **2020**, *367*, 1135.
[33] S. Kavadiya, A. Onno, C. C. Boyd, X. Wang, A. Cetta, M. D. McGehee, Z. C. Holman, *Solar RRL* **2021**, *5*, 2100107.
[34] N. Pant, M. Yanagida, Y. Shirai, K. Miyano, *Appl. Phys. Express* **2020**, *13*, 025505.
[35] N. Pant, A. Kulkarni, M. Yanagida, Y. Shirai, T. Miyasaka, K. Miyano, *Adv. Mater. Interfaces* **2020**, *7*, 1901748.
[36] N. Pant, A. Kulkarni, M. Yanagida, Y. Shirai, T. Miyasaka, K. Miyano, *ACS Appl. Energy Mater.* **2020**, *3*, 6215.
[37] C. C. Boyd, R. C. Shallcross, T. Moot, R. Kerner, L. Bertoluzzi, A. Onno, S. Kavadiya, C. Chosy, E. J. Wolf, J. Werner, J. A. Raiford, C. de Paula, A. F. Palmstrom, Z. J. Yu, J. J. Berry, S. F. Bent, Z. C. Holman, J. M. Luther, E. L. Ratcliff, N. R. Armstrong, M. D. McGehee, *Joule* **2020**, *4*, 1759.
[38] X. Wan, Y. Jiang, Z. Qiu, H. Zhang, X. Zhu, I. Sikandar, X. Liu, X. Chen, B. Cao, *ACS Appl. Energy Mater.* **2018**, *1*, 3947.
[39] Z. Saki, K. Sveinbjörnsson, G. Boschloo, N. Taghavinia, *ChemPhysChem* **2019**, *20*, 3322.
[40] C.-C. Diao, C.-Y. Huang, C.-F. Yang, C.-C. Wu, *Nanomaterials* **2020**, *10*, 636.
[41] C. M. Lin, C. C. Wu, *ACS Appl. Electron. Mater.* **2021**, *3*, 1050.
[42] H.-S. Kim, J.-Y. Seo, H. Xie, M. Lira-Cantu, S. M. Zakeeruddin, M. Grätzel, A. Hagfeldt, *ACS Omega* **2017**, *2*, 9074.
[43] X. Yin, J. Han, Y. Zhou, Y. Gu, M. Tai, H. Nan, Y. Zhou, J. Li, H. Lin, *J. Mater. Chem. A* **2019**, *7*, 5666.
[44] F. P. Gokdemir Choi, H. Moeini Alishah, S. Bozar, C. Kahveci, M. Canturk Rodop, S. Gunes, *Solar Energy* **2021**, *215*, 434.
[45] M. Feng, M. Wang, H. Zhou, W. Li, S. Wang, Z. Zang, S. Chen, *ACS Appl. Mater. Interfaces* **2020**, *12*, 50684.
[46] Y. Wang, T. Mahmoudi, Y.-B. Hahn, *Adv. Energy Mater.* **2020**, *10*, 2000967.
[47] Q. He, K. Yao, X. Wang, X. Xia, S. Leng, F. Li, *ACS Appl. Mater. Interfaces* **2017**, *9*, 41887.
[48] W. Chen, W. Chen, W. Chen, W. Chen, W. Chen, W. Chen, Y. Wu, J. Fan, A. B. Djurišić, F. Liu, H. W. Tam, A. Ng, C. Surya, W. K. Chan, W. K. Chan, D. Wang, Z. He, Z. He, *Adv. Energy Mater.* **2018**, *8*, 1703519.
[49] M. Feng, M. Wang, H. Zhou, W. Li, S. Wang, Z. Zang, S. Chen, *ACS Appl. Mater. Interfaces* **2020**, *12*, 50684.
[50] S. Akin, N. Arora, S. M. Zakeeruddin, M. Grätzel, R. H. Friend, M. I. Dar, *Adv. Energy Mater.* **2020**, *10*, 1903090.
[51] E. Aydin, M. De Bastiani, S. De Wolf, *Adv. Mater.* **2019**, *31*, 1900428.
[52] Y. Bai, H. Chen, S. Xiao, Q. Xue, T. Zhang, Z. Zhu, Q. Li, C. Hu, Y. Yang, Z. Hu, F. Huang, K. S. Wong, H.-L. Yip, S. Yang, *Adv. Funct. Mater.* **2016**, *26*, 2950.
[53] Y.-M. Chang, C.-W. Li, Y.-L. Lu, M.-S. Wu, H. Li, Y.-S. Lin, C.-W. Lu, C.-P. Chen, Y. J. Chang, *ACS Appl. Mater. Interfaces* **2021**, *13*, 6450.
[54] W. Chen, G. Pang, Y. Zhou, Y. Sun, F.-Z. Liu, R. Chen, S. Chen, A. B. Djurišić, Z. He, *J. Mater. Chem. A* **2020**, *8*, 1865.
[55] Z.-W. Gao, Y. Wang, D. Ouyang, H. Liu, Z. Huang, J. Kim, W. C. H. Choy, *Small Methods* **2020**, *4*, 2000478.
[56] W. Han, G. Ren, Z. Li, M. Dong, C. Liu, W. Guo, *J. Energy Chem.* **2020**, *46*, 202.
[57] C. Hu, Y. Bai, S. Xiao, K. Tao, W. K. Ng, K. S. Wong, S. H. Cheung, S. K. So, Q. Chen, S. Yang, *Solar RRL* **2020**, *4*, 2000270.
[58] X. Lian, J. Chen, S. Shan, G. Wu, H. Chen, *ACS Appl. Mater. Interfaces* **2020**, *12*, 46340.
[59] Z. Li, B. H. Jo, S. J. Hwang, T. H. Kim, S. Somasundaram, E. Kamaraj, J. Bang, T. K. Ahn, S. Park, H. J. Park, *Adv. Sci.* **2019**, *6*, 1802163.
[60] R. Li, P. Wang, B. Chen, X. Cui, Y. Ding, Y. Li, D. Zhang, Y. Zhao, X. Zhang, *ACS Energy Lett.* **2020**, *5*, 79.
[61] X. Liu, H. Wei Qiao, M. Chen, B. Ge, S. Yang, Y. Hou, H. Gui Yang, *Mater. Chem. Front.* **2021**, *5*, 3614.
[62] D. S. Mann, P. Patil, S.-N. Kwon, S.-I. Na, *Appl. Surf. Sci.* **2021**, *560*, 149973.
[63] N. Pant, A. Kulkarni, M. Yanagida, Y. Shirai, S. Yashiro, M. Sumiya, T. Miyasaka, K. Miyano, *ACS Appl. Energy Mater.* **2021**, *4*, 4530.
[64] G. Shen, Q. Cai, H. Dong, X. Wen, X. Xu, C. Mu, *ACS Sustainable Chem. Eng.* **2021**, *9*, 3580.
[65] S.-Y. Wang, C.-P. Chen, C.-L. Chung, C.-W. Hsu, H.-L. Hsu, T.-H. Wu, J.-Y. Zhuang, C.-J. Chang, H. M. Chen, Y. J. Chang, *ACS Appl. Mater. Interfaces* **2019**, *11*, 40050.
[66] Y. Wu, D. Wang, J. Liu, H. Cai, *Nanomaterials* **2021**, *11*, 775.
[67] X. Yin, J. Zhai, P. B. Ingabire, P. Du, W.-H. Chen, L. Song, J. Xiong, F. Ko, *Adv. Mater. Interfaces* **2021**, *8*, 2100862.
[68] X. Zheng, Z. Song, Z. Chen, S. S. Bista, P. Gui, N. Shrestha, C. Chen, C. Li, X. Yin, R. A. Awni, H. Lei, C. Tao, R. J. Ellingson, Y. Yan, G. Fang, *J. Mater. Chem. C* **2020**, *8*, 1972.
[69] S. Zhumagali, F. H. Isikgor, P. Maity, J. Yin, E. Ugur, M. De Bastiani, A. S. Subbiah, A. J. Mirabelli, R. Azmi, G. T. Harrison, J. Troughton, E. Aydin, J. Liu, T. Allen, A. ur Rehman, D. Baran, O. F. Mohammed, S. De Wolf, *Adv. Energy Mater.* **2021**, *11*, 2101662.
[70] D. Di Girolamo, F. Matteocci, F. U. Kosasih, G. Chistiakova, W. Zuo, G. Divitini, L. Korte, C. Ducati, A. Di Carlo, D. Dini, A. Abate, *Adv. Energy Mater.* **2019**, *9*, 1901642.
[71] M. Jošt, L. Kegelmann, L. Korte, S. Albrecht, *Adv. Energy Mater.* **2020**, *10*, 1904102.
[72] S. Khodabakhsh, D. Poplavskyy, S. Heutz, J. Nelson, D. D. C. Bradley, H. Murata, T. S. Jones, *Adv. Funct. Mater.* **2004**, *14*, 1205.
[73] P. J. Hotchkiss, H. Li, P. B. Paramonov, S. A. Paniagua, S. C. Jones, N. R. Armstrong, J.-L. Brédas, S. R. Marder, *Adv. Mater.* **2009**, *21*, 4496.

[74] Y. Ogomi, A. Morita, S. Tsukamoto, T. Saitho, Q. Shen, T. Toyoda, K. Yoshino, S. S. Pandey, T. Ma, S. Hayase, *J. Phys. Chem. C* **2014**, *118*, 16651.
[75] K. Wojciechowski, S. D. Stranks, A. Abate, G. Sadoughi, A. Sadhanala, N. Kopidakis, G. Rumbles, C.-Z. Li, R. H. Friend, A. K.-Y. Jen, H. J. Snaith, *ACS Nano* **2014**, *8*, 12701.
[76] H. Bin Kim, I. Im, Y. Yoon, S. Do Sung, E. Kim, J. Kim, W. In Lee, *J. Mater. Chem. A* **2015**, *3*, 9264.
[77] K. Liu, S. Chen, J. Wu, H. Zhang, M. Qin, X. Lu, Y. Tu, Q. Meng, X. Zhan, *Energy Environ. Sci.* **2018**, *11*, 3463.
[78] J. Will, Y. Hou, S. Scheiner, U. Pinkert, I. M. Hermes, S. A. Weber, A. Hirsch, M. Halik, C. Brabec, T. Unruh, *ACS Appl. Mater. Interfaces* **2018**, *10*, 5511.
[79] A. Al-Ashouri, E. Köhnen, B. Li, A. Magomedov, H. Hempel, P. Caprioglio, J. A. Márquez, A. B. Morales Vilches, E. Kasparavicius, J. A. Smith, N. Phung, D. Menzel, M. Grischek, L. Kegelmann, D. Skroblin, C. Gollwitzer, T. Malinauskas, M. Jošt, G. Matič, B. Rech, R. Schlatmann, M. Topič, L. Korte, A. Abate, B. Stannowski, D. Neher, M. Stolterfoht, T. Unold, V. Getautis, S. Albrecht, *Science* **2020**, *370*, 1300.
[80] A. S. Subbiah, F. H. Isikgor, C. T. Howells, M. De Bastiani, J. Liu, E. Aydin, F. Furlan, T. G. Allen, F. Xu, S. Zhumagali, S. Hoogland, E. H. Sargent, I. McCulloch, S. De Wolf, *ACS Energy Lett.* **2020**, *5*, 3034.
[81] I. Levine, A. Al-Ashouri, A. Musiienko, H. Hempel, A. Magomedov, A. Drevilkauskaite, V. Getautis, D. Menzel, K. Hinrichs, T. Unold, S. Albrecht, T. Dittrich, *Joule* **2021**, *5*, 2915.
[82] N. Phung, M. Verheijen, A. Todinova, K. Datta, M. Verhage, A. Al-Ashouri, H. Köbler, X. Li, A. Abate, S. Albrecht, M. Creatore, *ACS Appl. Mater. Interfaces* **2022**, *14*, 2166.
[83] I. Kafedjiska, G. A. Farias-Basulto, P. Reyes-Figueroa, T. Bertram, A. Al-Ashouri, C. A. Kaufmann, R. Wenisch, S. Albrecht, R. Schlatmann, I. Lauermann, *Sol. Energy Mater. Sol. Cells* **2023**, *254*, 112248.
[84] I. Kafedjiska, G. A. Farias Basulto, F. Ruske, N. Maticiuc, T. Bertram, C. Kaufmann, R. Schlatmann, I. Lauermann, *J. Phys.* **2023**, *5*, 024014.
[85] E. Climent-Pascual, B. C. Hames, J. S. Moreno-Ramírez, A. L. Álvarez, E. J. Juarez-Perez, E. Mas-Marza, I. Mora-Seró, A. De Andrés, C. Coya, *J. Mater. Chem. A* **2016**, *4*, 18153.
[86] T. Fellmeth, F. Clement, D. Biro, *IEEE J. Photovoltaics* **2014**, *4*, 504.
[87] W. E. McMahon, K. E. Emery, D. J. Friedman, L. Ottoson, M. S. Young, J. S. Ward, C. M. Kramer, A. Duda, S. Kurtz, *Prog. Photovoltaics* **2008**, *16*, 213.
[88] C. Ulbrich, C. Zahren, A. Gerber, B. Blank, T. Merdzhanova, A. Gordijn, U. Rau, *Int. J. Photoenergy* **2013**, *2013*, e314097.
[89] E. Köhnen, M. Jošt, A. B. Morales-Vilches, P. Tockhorn, A. Al-Ashouri, B. Macco, L. Kegelmann, L. Korte, B. Rech, R. Schlatmann, B. Stannowski, S. Albrecht, *Sustainable Energy Fuels* **2019**, *3*, 1995.
[90] T. Dittrich, S. Fengler, *Surface Photovoltage Analysis of Photoactive Materials*, World Scientific, New Jersey **2020**.
[91] T. Kirchartz, J. A. Márquez, M. Stolterfoht, T. Unold, *Adv. Energy Mater.* **2020**, *10*, 1904134.
[92] Y. Hou, X. Chen, S. Yang, C. Li, H. Zhao, H. G. Yang, *Adv. Funct. Mater.* **2017**, *27*, 1700878.
[93] S. Y. Kim, S. J. Cho, S. E. Byeon, X. He, H. J. Yoon, *Adv. Energy Mater.* **2020**, *10*, 2002606.
[94] P.-Y. Gu, N. Wang, C. Wang, Y. Zhou, G. Long, M. Tian, W. Chen, X. W. Sun, M. G. Kanatzidis, Q. Zhang, *J. Mater. Chem. A* **2017**, *5*, 7339.
[95] C. M. Wolff, P. Caprioglio, M. Stolterfoht, D. Neher, *Adv. Mater.* **2019**, *31*, 1902762.
[96] A. Buin, P. Pietsch, J. Xu, O. Voznyy, A. H. Ip, R. Comin, E. H. Sargent, *Nano Lett.* **2014**, *14*, 6281.
[97] P. Schulz, D. Cahen, A. Kahn, *Chem. Rev.* **2019**, *119*, 3349.
[98] K. Choi, H. Choi, J. Min, T. Kim, D. Kim, S. Y. Son, G.-W. Kim, J. Choi, T. Park, *Solar RRL* **2020**, *4*, 1900251.
[99] M. D. Heinemann, R. Mainz, F. Österle, H. Rodriguez-Alvarez, D. Greiner, C. A. Kaufmann, T. Unold, *Sci. Rep.* **2017**, *7*, 45463.
[100] T. Kodalle, M. D. Heinemann, D. Greiner, H. A. Yetkin, M. Klupsch, C. Li, P. A. van Aken, I. Lauermann, R. Schlatmann, C. A. Kaufmann, *Solar RRL* **2018**, *2*, 1800156.
[101] R. Ortega-Borges, D. Lincot, *J. Electrochem. Soc.* **1993**, *140*, 3464.
[102] M. Saliba, T. Matsui, J.-Y. Seo, K. Domanski, J.-P. Correa-Baena, M. K. Nazeeruddin, S. M. Zakeeruddin, W. Tress, A. Abate, A. Hagfeldt, M. Grätzel, *Energy Environ. Sci.* **2016**, *9*, 1989.
[103] I. Lauermann, A. Steigert, *JLSRF* **2016**, *2*, A67.